NATIONAL ENERGY TECHNOLOGY LABORATORY

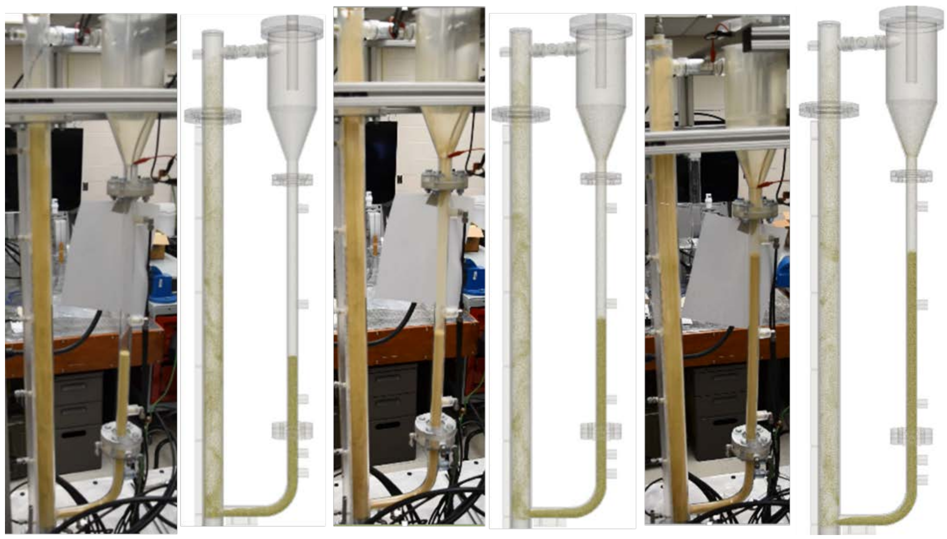

# Numerical simulation of a full-loop circulating fluidized bed under different operating conditions

June 2017

Office of Fossil Energy

NETL-PUB-21290

# Disclaimer

This report was prepared as an account of work sponsored by an agency of the United States Government. Neither the United States Government nor any agency thereof, nor any of their employees, makes any warranty, express or implied, or assumes any legal liability or responsibility for the accuracy, completeness, or usefulness of any information, apparatus, product, or process disclosed, or represents that its use would not infringe privately owned rights. Reference therein to any specific commercial product, process, or service by trade name, trademark, manufacturer, or otherwise does not necessarily constitute or imply its endorsement, recommendation, or favoring by the United States Government or any agency thereof. The views and opinions of authors expressed therein do not necessarily state or reflect those of the United States Government or any agency thereof.

**Cover Illustration:** Direct comparison between simulation and experiments

(Left: Experiment, Right: Simulation)

**Suggested Citation:** Xu, Y.; Musser, J.; Li, T.; Rogers, W.A. *Numerical simulation of a full-loop circulating fluidized bed under different operating conditions*; NETL-PUB-21290; NETL Technical Report Series; U.S. Department of Energy, National Energy Technology Laboratory: Morgantown, WV, 2017; p 50.

# Numerical simulation of a full-loop circulating fluidized bed under different operating conditions

**Yupeng Xu[1], Jordan Musser[1], Tingwen Li[1,2], William A. Rogers[1]**

**[1] National Energy Technology Laboratory, Morgantown, WV 26505, USA**

**[2] AECOM, Morgantown, WV 26505, USA**

---

**NETL-PUB-21290**

28 June 2017

NETL Contacts:

Jordan Musser, Principal Investigator

David E. Alman, Executive Director, Research and Innovation Center

# Table of Contents

1. INTRODUCTION....2
2. METHODS....4
3. OBSERVATIONS....11
4. CONCLUSIONS....37
5. REFERENCES....38

# List of Figures

Figure 1: (a) Snapshot of experimental setup; (b)Schematic representation of the circulating fluidized bed; (c) Geometric configuration and (d) grid representation deployed in the simulations. ........ 9
Figure 2: Average solids holdup along the riser (simulated data were taken from the center line across the riser) (a) Systems with different grid resolutions; (b) systems with different statistical time. ........ 10
Figure 3: Predicted, time-averaged pressure profile around the CFB system. ........ 12
Figure 4: Comparison of measured and predicted time-averaged pressure drop across key system components. ........ 12
Figure 5: Solids circulation rate predicted by different drag correlations. ........ 14
Figure 6: Instantaneous solids standpipe inventory height under different drag correlations. ........ 15
Figure 7: Predicted solids volume fraction in the CFB system. ........ 16
Figure 8: Time-averaged gas void fraction along longitudinal cross section of riser under different drag correlations (the height of riser is scaled down for better representation) (a) BVK (b) Gidaspow (c) HKL (d) Wen&Yu. ........ 17
Figure 9: The typical core-annulus structure (the average vertical particle velocity) along the riser with the HKL drag correlation. ........ 18
Figure 10: The average radial solids volume fraction at 4 different heights (a) 0.25 m, (b) 0.50 m, (c) 0.75 m, (d) 1.00 m. Note R is the radius of the riser and r/R is the dimensionless radial direction ........ 21
Figure 11: Trajectory of a tracer particle inside the CFB and the division of the system for the calculation of the residence times. ........ 21
Figure 12: Residence time distribution in different components of the CFB under different drag correlations: (a) BVK (b) Gidaspow (c) HKL (d) Wen&Yu. ........ 22
Figure 13: Particle size distribution. Sim = used in simulation; Exp = measured values ........ 23
Figure 14: Comparison of measured and predicted time-averaged pressure drop across key system components (Mono disperse and PSD). ........ 24
Figure 15: Solids circulation rate with and without particle size distribution. ........ 25
Figure 16: Solids standpipe inventory height. ........ 26
Figure 17: Direct comparison between experiments and simulations under different operating conditions. ........ 27
Figure 18: Direct comparison of pressure drop at different locations under all 3 operation conditions. ........ 29
Figure 19: Direct comparison of the solids standpipe inventory height under different operation conditions. ........ 30
Figure 20: Average solid holdup along the riser under different operation conditions. ........ 31
Figure 21: Time-averaged gas void fraction of the center surface inside the riser under different drag correlations. ........ 32
Figure 22: Influence of different operating conditions on instantaneous solid velocity. Shown are radial cross sections of the CFB riser at indicated heights (h) from the inlet ........ 33
Figure 23: The average radial solids volume fraction at 4 different heights (a) 1.00 m, (b) 0.75 m, (c) 0.50 m, (d) 0.25 m under 3 different operation conditions, here r/R is the dimensionless radial direction. ........ 35

Figure 24: Residence time distribution through different components of the CFB under 3 different operating conditions. ........ 36

# List of Tables

Table 1: Parameters used for the simulations and fluidization experiments ........ 7
Table 2: Gas flow rates in standard liters per minute (SLPM) at three different injection sites (see Figure 1B) under 3 operating conditions ........ 8
Table 3: Observed experimental and predicted mean solids circulation rates ........ 13
Table 4: Observed experimental and predicted mean solids standpipe inventory height ........ 15
Table 5: Solids circulation rate ........ 29
Table 6: Standpipe bed height ........ 30

# Acronyms, Abbreviations, and Symbols

| Term | Description |
| --- | --- |
| CFB | Circulating Fluidized Bed |
| CFD | Computational Fluid Dynamics |
| TFM | Two Fluid Model |
| DEM | Discrete Element Method |
| DNS | Direct Numerical Simulation |
| SLPM | Standard liter per minute |
| HDPE | High-density polyethylene |
| PIV | Particle Image Velocimetry |

# Acknowledgments

This work was completed as part of National Energy Technology Laboratory (NETL) research for the U.S. Department of Energy's (DOE) Carbon Storage Program. The authors wish to acknowledge Balaji Gopalan, Rupen Panday, Jonathan Tucker, Greggory Breault for providing experimental data for validation and also thank Mary Ann Clarke for her help in improving the manuscript.

## ABSTRACT

Both experimental and computational studies of the fluidization of high-density polyethylene (HDPE) particles in a small-scale full-loop circulating fluidized bed are conducted. Experimental measurements of pressure drop are taken at different locations along the bed. The solids circulation rate is measured with an advanced Particle Image Velocimetry (PIV) technique. The bed height of the quasi-static region in the standpipe is also measured. Comparative numerical simulations are performed with a Computational Fluid Dynamics solver utilizing a Discrete Element Method (CFD-DEM). This paper reports a detailed and direct comparison between CFD-DEM results and experimental data for realistic gas-solid fluidization in a full-loop circulating fluidized bed system. The comparison reveals good agreement with respect to system component pressure drop and inventory height in the standpipe. In addition, the effect of different drag laws applied within the CFD simulation is examined and compared with experimental results.

## 1. INTRODUCTION

Circulating fluidized beds (CFB) are used in industry for a wide variety of gas-solid contact operations. Examples include coal and biomass gasification/combustion, catalytic cracking and Fischer-Tropsch synthesis. The extensive application of CFBs to industrial processes drives investment, and consequently increases interest in their operational productivity. A detailed understanding of gas–solid hydrodynamics in fluidized beds can be utilized to improve their design and operation.

Over the past few decades, CFB hydrodynamics, including circulation patterns, have been studied using various costly and time-consuming experimental approaches. Intrusive techniques including optical probes (Reh and Li, 1991), endoscopes (Werther, 1999; Lackermeier et al., 2001) and hot wires (Boerefijn et al., 1999) have been employed to collect cross-sectional porosity data from fluidized beds. Non-intrusive methods for data collection include electrical capacitance tomography (Zhang et al., 2014), laser Doppler anemometry (Mathiesen et al., 2000), phase Doppler anemometry (Levy and Lockwood, 1983), magnetic resonance imaging (Müller et al., 2008), magnetic particle tracking (Mohs et al., 2009; Buist et al., 2014) and particle image velocimetry (PIV) (Carlos Varas et al., 2016). All of these technologies can provide accurate measurements of particle data, but PIV is among the most reliable and economical techniques (Carlos Varas et al., 2016). Through the analysis of data from such experimental techniques, many hydrodynamic characteristics in CFBs have been revealed. A core-annulus structure (Bader et al., 1988; Li et al., 1988; Miller and Gidaspow, 1992), an "S-shape" axial profile (Li et al., 1988; Louge and Chang, 1990), particle clusters (Yerushalmi et al., 1976; Ishii et al., 1989; Horio and Kuroki, 1994), residence time distribution (RTD) (Ambler et al., 1990; Patience and Chaouki, 1993), as well as entry and exit effects (Bai et al., 1992; Brereton and Grace, 1993; Pugsley et al., 1997; Cheng et al., 1998) are among the many documented discoveries.

Numerical simulation is a powerful tool for modeling gas–solid motion. Computational studies employing various models have been used to predict the performance of fluidized systems at different scales. An Eulerian two-fluid model (TFM), an Eulerian fluid model coupled with a Lagrangian Discrete Element Method for particles (CFD-DEM), and direct numerical simulation (DNS) are examples. In the TFM, a continuum description is employed for both the solid and gas phases. The TFM is capable of predicting flow behavior of gas-solid systems at large scale, but it relies on closure relations for effective solids pressure and viscosity (Lun et al., 1984). In CFD-DEM, particle motion is computed using Newton's second law; collisional forces and gas-particle interactions are accounted to capture flow features such as clusters. Also, particle-scale information including residence time, collision forces, and dispersion intensities are available for detailed analyses of complex flow phenomena. However, compared to TFM simulations, computational expense is higher, historically limiting the application of CFD-DEM to small scale systems. Today, parallelization of CFD-DEM codes enables large scale simulations with hundreds of millions of particles (Walther and Sbalzarini, 2009; Jajcevic et al., 2013; Yang et al., 2015; Tsuzuki and Aoki, 2016). Finally, DNS fully resolves the no-slip boundary condition at the surface of each particle (HILL et al., 2001; van der Hoef et al., 2006; Beetstra et al., 2007). This level of refinement is more computationally expensive than CFD-DEM and further limits the total particle number that can be simulated.

Much past research focuses on the numerical simulation of gas–solid motion in singular parts of a CFB (Wang et al., 2008; Li et al., 2014). However, only few report numerical analyses of full-loop CFBs. For example, Zhang et al. (Zhang et al., 2010) performed a three-dimensional full-loop computational simulation of the hydrodynamics in a CFB boiler using an Eulerian granular multiphase model. They captured the non-uniform distribution of solid flux in the two cyclones. Nikolopoulos et al. (Nikolopoulos et al., 2013) reported a full-loop isothermal simulation of the hydrodynamics in a CFB reactor by means of TFM. Likewise, using an Eulerian multiphase model, Lu et al. (Lu et al., 2013) investigated the hydrodynamic behaviors of gas and solid phases in an industrial-scale CFB boiler with and without a fluidized bed heat exchanger. While these studies are important, they lack information related to particle residence time, the contact force between colliding particles, and dispersion intensity, quantities which are crucial to the design and optimization of a CFB. However, these important particle-scale details can be obtained with CFD-DEM. To the authors' knowledge, there is rare particle-scale level work published for both physically and numerically modelled full-loop CFBs.

In this work, a small scale, full-loop CFB is investigated using physical experiments and CFD-DEM simulations. The numerical simulations utilize the U.S. Department of Energy's Multiphase Flow with Interphase eXchanges code, MFIX. Experimental and simulation results are compared using pressure drop, solids circulation rate and solids standpipe inventory height data. Additionally, the performance of different drag laws is examined within the MFIX-DEM framework.

# 2. METHODS

## 2.1 Simulation methods

In this study, the Multiphase Flow with Interphase eXchanges (MFIX) code, freely available from the U.S. Department of Energy (DOE), National Energy Technology Laboratory (NETL) at https://mfix.netl.doe.gov, was used. MFIX is a general-purpose computer code for modeling the hydrodynamics, heat transfer and chemical reactions in fluid-solids systems. In MFIX-DEM, a CFD flow solver is coupled with a DEM to simulate gas-solid flow (Syamlal et al., 1993, 2012; Syamlal, 1998; Garg et al., 2012; Li et al., 2012). Gas flow is modeled by the averaged Navier-Stokes equations for mass and momentum conservation, while the motion of particles is described by Newton's equations of motion. The MFIX-DEM governing equations and key closure models used in this work are detailed below.

### 2.1.1 Equations of motion for the particles

In DEM, the position, linear and angular velocities of each particle are tracked. The translational and rotational motion of particle $\boldsymbol{i}$ with mass $\boldsymbol{m_i}$, moment of inertia $\boldsymbol{I_i}$ and coordinate $\mathbf{r_i}$ can be described by Newton's equations for rigid body motion

$$m_i \frac{d^2\mathbf{r}_i}{dt^2} = \mathbf{F}_{g,i} + \mathbf{F}_{c,i} + \mathbf{F}_{p,i} + \mathbf{F}_{d,i} \tag{1}$$

$$I_i \frac{d\boldsymbol{\omega}_i}{dt} = \mathbf{T}_i \tag{2}$$

The four terms on the right-hand side of (1) account for the gravitational force, the sum of the individual contact forces exerted by all other particles in contact with particle $i$, the pressure gradient force induced by pressure difference, and the drag force induced by the relative velocity between the particles and local gas velocity, respectively. In (2), $\boldsymbol{\omega}_i$, is angular velocity and $\mathbf{T}_i$ is torque around the center-of-mass of particle $i$ due to particle collision forces. Two types of collision models are widely used, namely the hard sphere model and the soft sphere model. In our simulation, the soft sphere model is used since the hard sphere model is not suited for systems where quasi-static particle configurations exist. More detailed information can be found in (Alder and Wainwright, 1957; van der Hoef et al., 2006).

For the calculation of $\mathbf{F}_{c,i}$, a linear spring and dashpot soft-sphere collision model along the lines of Cundall and Strack is used (van Sint Annaland et al., 2005; Xiong et al., 2012). In this model, the total contact force on particle $i$ of radius $R_i$ is given by a sum of normal and tangential pair forces with neighboring particles in contact,

$$\mathbf{F}_{c,i} = \sum_{j\in\Im}\left(\mathbf{F}_{n,ij} + \mathbf{F}_{t,ij}\right) \tag{3}$$

where $\Im$ is the set of particles in contact with particle $i$. The normal forces $\mathbf{F}_{n,ij}$ between two particles *i* and *j* can be calculated by

$$\mathbf{F}_{n,ij} = -k_n \delta_n \mathbf{n}_{ij} - \eta_n \mathbf{V}_{n,ij} \tag{4}$$

Where $k_n$ is normal spring stiffness, and $\eta_n$ is normal damping coefficient. The normal force depends linearly on the overlap, $\delta_n = R_i + R_j - |\mathbf{r}_i - \mathbf{r}_j|$, and relative normal velocity,

$\mathbf{V}_{n,ij} = (\mathbf{V}_{ij} \cdot \mathbf{n}_{ij})\mathbf{n}_{ij}$, where $\mathbf{n}_{ij}$ is the unit vector pointing from the center of $j$ to the center of $i$. $\mathbf{V}_{ij}$ is the relative velocity of particles $i$ and $j$, which is

$$\mathbf{V}_{ij} = (\mathbf{V}_i - \mathbf{V}_j) + (R_i \boldsymbol{\omega}_i + R_j \boldsymbol{\omega}_j) \times \mathbf{n}_{ij} \tag{5}$$

Where $\mathbf{V_i}$ and $\mathbf{V}_j$ are particles velocities, and $\boldsymbol{\omega}_i$ and $\boldsymbol{\omega}_j$ are the angular velocities.

The tangential component of the contact force is given as

$$\mathbf{F}_{t,ij} = \begin{cases} -k_t \delta_t \mathbf{t}_{ij} - \eta_t \mathbf{V}_{t,ij} & for\ |\mathbf{F}_{t,ij}| \le \mu_f |\mathbf{F}_{n,ij}| \\ -\mu_f |\mathbf{F}_{n,ij}| \mathbf{t}_{ij} & for\ |\mathbf{F}_{t,ij}| > \mu_f |\mathbf{F}_{n,ij}| \end{cases} \tag{6}$$

Note that $k_t$ is tangential spring stiffness, $\delta_t$ is tangential displacement, $\eta_t$ is tangential damping coefficient, $\mathbf{V}_{t,ij}$ is tangential relative velocity, $\mu_f$ is friction coefficient, and $\mathbf{t}_{ij}$ is the tangential unit vector. The tangential relative velocity is

$$\mathbf{V}_{t,ij} = \mathbf{V}_{ij} - \mathbf{V}_{n,ij} \tag{7}$$

and the tangential unit vector, $\mathbf{t}_{ij}$ is defined as

$$\mathbf{t}_{ij} = \frac{\mathbf{V}_{t,ij}}{|\mathbf{V}_{t,ij}|} \tag{8}$$

The tangential forces also lead to a torque force on the particles:

$$\mathbf{T}_i = \sum_{j \in \Im} (R_i \mathbf{n}_{ij} \times \mathbf{F}_{t,ij}) \tag{9}$$

The pressure gradient force, $\mathbf{F}_{p,i}$, is evaluated as

$$\mathbf{F}_{p,i} = -\nabla P_g(\mathbf{r}_i) V_i \tag{10}$$

Where $V_i$ is the total volume of particle $i$ and $\nabla P_g(\mathbf{r}_i)$ stands for the local pressure gradient of the gas phase across the particle $i$.

$\mathbf{F}_{d,i}$ is the gas phase drag force exerted on particle $i$ given by

$$\mathbf{F}_{d,i} = \frac{\beta_i V_i}{\varepsilon_s}\left(\mathbf{u}_g - \mathbf{V}_p\right) \tag{11}$$

Where $\varepsilon_s$ is the solids volume fraction in the computational cell in which the particle is located. $\mathbf{u}_g$ and $\mathbf{V}_p$ are the gas phase and solid phase velocity vectors in the cell, and $\beta_i$ is the interphase momentum exchange coefficient for particle *i*, which is calculated using empirical correlations. In this work, the effect of different empirical correlations including BVK (Beetstra et al., 2007), Gidaspow (Ding and Gidaspow, 1990), Koch-Hill-Ladd (HILL et al., 2001) and Wen&Yu (Wen and Yu, 1966) are evaluated.

### 2.1.2 Governing equations for the gas phase

The gas phase flow field is computed from the volume-averaged Navier-Stokes equations given by:

$$\frac{\partial}{\partial t}\left(\varepsilon_g \rho_g\right) + \nabla \cdot \left(\varepsilon_g \rho_g \mathbf{u}_g\right) = 0 \tag{12}$$

$$\frac{\partial}{\partial t}\left(\varepsilon_g \rho_g \mathbf{u}_g\right) + \nabla \cdot \left(\varepsilon_g \rho_g \mathbf{u}_g \mathbf{u}_g\right) = -\varepsilon_g \nabla P_g - \nabla \cdot \left(\varepsilon_g \tau_g\right) - \mathbf{S}_p + \varepsilon_g \rho_g \boldsymbol{g} \tag{13}$$

Where $\varepsilon_g$ is the local gas volume fraction, $\rho_g$ is gas phase density, $\mathbf{u}_g$ is gas velocity, $P_g$ is gas pressure, $\tau_g$ is the viscous stress tensor, $\boldsymbol{g}$ is gravitational acceleration, and $\mathbf{S}_p$ is a source term that accounts for the momentum exchange with the solid particles. $\mathbf{S}_p$ is computed from:

$$\mathbf{S}_p = \frac{1}{V}\sum_{i}^{n} \frac{\beta_i V_i}{\varepsilon_s}\left(\mathbf{u}_g(\mathbf{r}_i) - \mathbf{V}_{p,i}\right) \tag{14}$$

The fluid density is determined using the ideal gas law, and the viscous stress tensor is assumed to obey the general form for a Newtonian fluid.

$$\tau_g = -\left[\left(\lambda_g - \frac{2}{3}\mu_g\right)\left(\nabla \cdot \mathbf{u}_g\right)\mathbf{I} + \mu_g\left(\left(\nabla \mathbf{u}_g\right) + \left(\nabla \mathbf{u}_g\right)^T\right]\right. \tag{15}$$

Full details on the governing equations along with the numerical implementation and coupling procedure can be found in Garg et al. (Garg et al., 2012; Li et al., 2012).

## 2.2 Experimental techniques

In the current work, the investigated apparatus is a 3D-printed, lab-scale CFB consisting of a cylindrical riser, cyclone, standpipe and L-valve. It is made from clear acrylic pieces, thus the dynamics of gas-particle flow can be visualized clearly. The objective of the physical experiments was to collect comparative data for the hydrodynamic numerical study of the gas-solids flow in the CFB. The geometric configuration of the investigated CFB is illustrated in Fig. 1 (a). The riser has a height of 1.32 m, and the internal diameters of the cyclone, riser and standpipe are 0.127 m, 0.0508 m and 0.0254 m, respectively. The CFB was filled with 350 g of High Density Polyethylene

(HDPE) beads (physical properties in Table 1). The gas flow inside the bed was controlled through three mass flow controllers that were supplied via a 690 kPa air header as shown in Fig.1 (b).

It was quickly noted that the experimental set-up created static charge in dry operation. An anti-static agent was sought to alleviate the problem. However, to distribute said agent, before each experiment, a mixture of water and anti-static agent had to be foamed through the system. Subsequently, the unit was dried with air. The process for managing the anti-static agent is now detailed.

During start-up, the CFB riser was charged with a mixture of water vapor and the anti-static agent, *Larostat*, along with air for 15-20 seconds. The air's physical properties are detailed in Table 1. The choice between 15 or 20 seconds depended upon the visual observation of foaming in a clear plenum section. Once the anti-static agent was fully applied, the CFB was circulated with dry air to eliminate the added moisture in the system.

When the system was dry, air was supplied to the CFB with flow rates as specified in the test matrix shown in Table 2. Note that the test conditions reflect a generic range of solids flux from dilute to dense. A system steady-state was defined when a constant pressure differential was maintained across the riser, and standpipe bed height was stable. System steady-state was held for 10 minutes for each test setting before measurements were obtained. Measurements included pressure drop, solids flux and the standpipe bed height. Experiments were conducted with two independent variables including gas flow rate at the distributor and the aerations at the return leg of a CFB.

Experimental techniques employed in the experiments will be briefly presented hereafter and more details can be found in the corresponding experimental tech report titled "Experimental Measurements of Small-Scale Circulating Fluidized Bed Performance for Model Validation" (Panday et al., 2017).

**Table 1: Parameters used for the simulations and fluidization experiments**

| Parameters | Simulations | Experiments |
|---|---|---|
| Particle density, $\rho_p$ | 863 kg/m$^3$ | 863 kg/m$^3$ |
| Particle diameter, $d_p$ | 871 µm | 871 µm |
| Particle mass, m | 350 g | 350 g |
| Gas density, $\rho_g$ | 1.2 kg/m$^3$ | Air |
| Gas viscosity, $\mu_g$ | 1.8*10$^{-5}$ kg/(m-s) | Air |

### 2.2.1 Pressure drop

Differential pressure measurements were made with Rosemount 1151DP Smart transmitters. The accuracy of these transmitters is within ± 0.075% of their calibrated span. The loop-powered Rosemount 1151DP measures the difference of pressures applied between 2 ports. A pressure difference between ports causes the instrument's internal diaphragm to deflect, resulting in a change in capacitance that is measured. The output is communicated through a 4-20 mA signal converted to 1-5 Volts through a 250 ohms resistor to the data acquisition system. The electrical signal is then scaled to the proper engineering units. In these experiments, the differential pressure was measured between different locations of the riser, crossover, cyclone, standpipe, L-valve and outlet as can be seen in Fig. 1(b).

Signal resolution is high enough to capture pressure fluctuations at all given operating conditions in these experiments. Note that pressure drop measurement is considered one of the most reliable approaches for determining axial solid distribution in a circulating fluidized bed system (Berruti et al., 1995).

### 2.2.2 High-speed Particle Image Velocimetry (HsPIV)

The HsPIV system with particle tracking, developed by NETL was utilized to acquire solid circulation rate presented in this work (Gopalan and Shaffer, 2012; Shaffer, 2013). A novel patented particle tracking algorithm (Shaffer, 2013) was used to extract individual particle information including particle velocity, density and trajectory from recorded images. The exact details of the tracking procedure are available elsewhere (Gopalan and Shaffer, 2013; Shaffer et al., 2013).

The solids flux was measured using HsPIV in the standpipe of the CFB. Low solid fluxes were measured by directly counting the number of particles that crossed a section of standpipe within a set time. Higher solids fluxes were calculated from measured velocity and estimated concentration using the high-speed video from HsPIV and an in-house calibration procedure. The measurement technique was validated in a half scale CFB facility where the L-valve was separated from the standpipe. In this configuration, particles fell onto a scale and were weighed directly. Combined with experimental time, this value was then extended to a solids flux. Measurement accuracy was determined to be ± 1% for low solids flux and ± 15% for higher solids fluxes.

### 2.2.3 High Speed video

The solids standpipe inventory height was measured using a high-speed camera and automated image processing software, ImageJ. Note that ImageJ is an open source image processing program designed for scientific multi-dimensional images.

**Table 2: Gas flow rates in standard liters per minute (SLPM) at three different injection sites (see Figure 1B) under 3 operating conditions**

| Operating Condition (SLPM) | Flow Controller FTC180 | Flow Controller FTC135 | Flow Controller FTC115 |
|---|---|---|---|
| Case 1 | 275 | 6 | 1.5 |
| Case 2 | 300 | 7.5 | 2.5 |
| Case 3 | 325 | 6 | 1.5 |

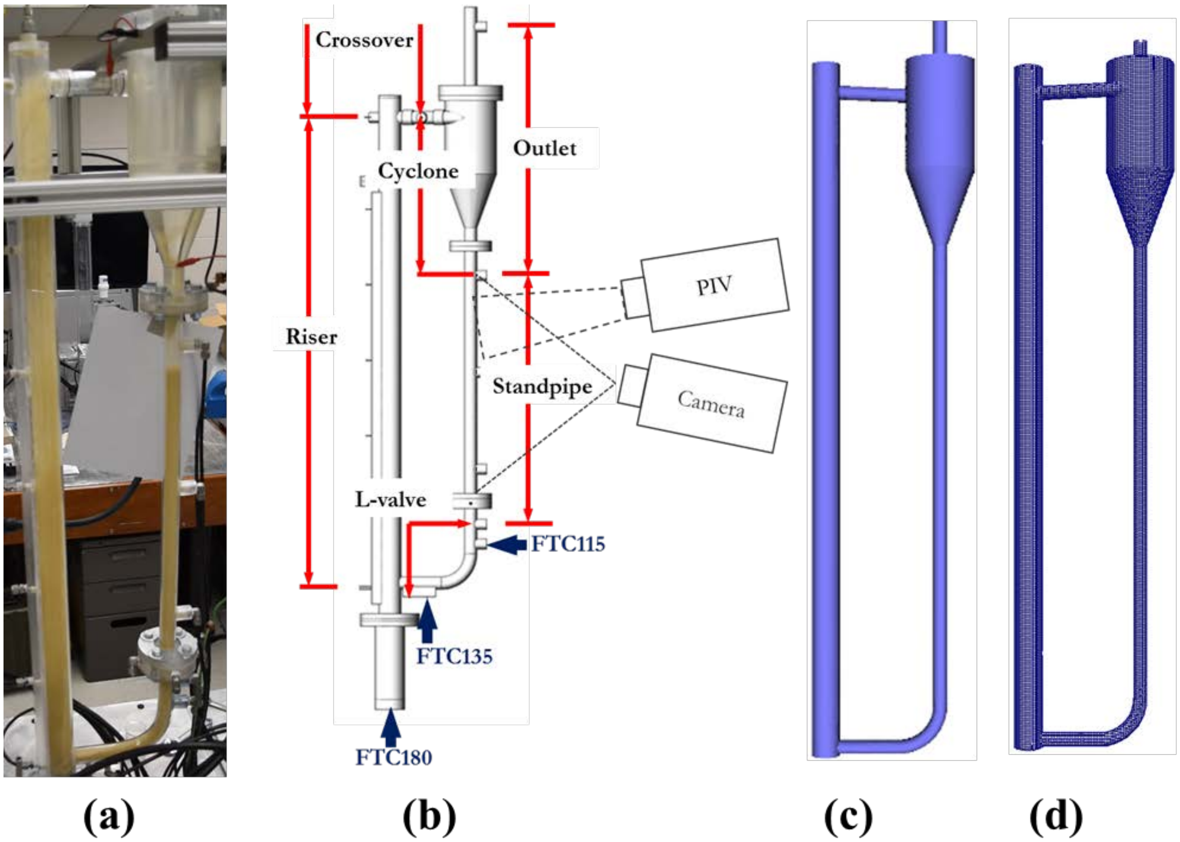


**Figure 1: (a) Snapshot of experimental setup; (b) Schematic representation of the circulating fluidized bed; (c) Geometric configuration and (d) grid representation deployed in the simulations.**

### 2.3 Experimental/simulation set-ups

The blocked simulation domain (W, H, D) is (0.32 m, 1.32 m, 0.15 m). Gas enters the riser from the bottom at FTC180, with a prescribed inlet velocity and exits the system through a pressure outlet on top of the cyclone. Besides the main gas inlet, two aeration gas inlets are introduced along the L-valve, FTC135 and FTC115 (see Figure 1b). A no-slip wall boundary condition is used for the gas phase. The MFIX Cartesian grid cut-cell technique is used to specify the geometry. In this approach, a Cartesian grid is used to discretize the computational domain while boundary cells are truncated to conform to the CFB internal surface. Details on the Cartesian grid cut-cell method can be found elsewhere (Kirkpatrick et al., 2003; Dietiker et al., 2009; Dietiker, 2015) . Simulations were run in parallel using a message passing interface (MPI) and open multi-processing (OpenMP) on NETL's supercomputer, Joule (Gopalakrishnan and Tafti, 2013; Liu et al., 2014).

A total of 350 g of HDPE particles with diameter = 0.871 mm and density = 863 kg/m$^3$ are tracked in the system. The physical properties of the bed material are characterized in Table 1. Following ISO Standard 13322-2, size and shape measurements were obtained using a SympaTEC — QICPIC particle analyzer that utilized dynamic image analysis. The particle diameter used in the simulations was the Sauter mean diameter, defined as the diameter of a sphere that has the same volume to surface area ratio as the actual particle of interest. The implementation of a full particle size distribution is planned for future simulations. Absolute density of the particles was obtained using a Micrometrics — AccuPyc 1330 Helium Pycnometer.

A simplistic grid independence study was conducted with results given in Figure 2(a). The fine grid has 1,003,200 cells (80x330x38) and the coarse grid has 132,000 grid cells (40x165x20). Figure 2(a) illustrates the cross-sectional averaged solids holdup along the riser with the different grid resolutions. No systematic difference appears in the simulation results obtained using different grid resolutions, but finer grid predicts smoother flow behavior at the bottom solids inlet and at the top exit of the riser. All later discussions are based on results obtained with the fine grid.

The total simulated time was around 25 s. In post-processing, the first 10 s were discarded to exclude start-up effects. Beyond 10 s, pseudo-steady state was attained. Figure 2(b) illustrates the cross-sectional averaged solids holdup along the riser utilizing time averaging. One can see that the curves generally overlap regardless of average time set.

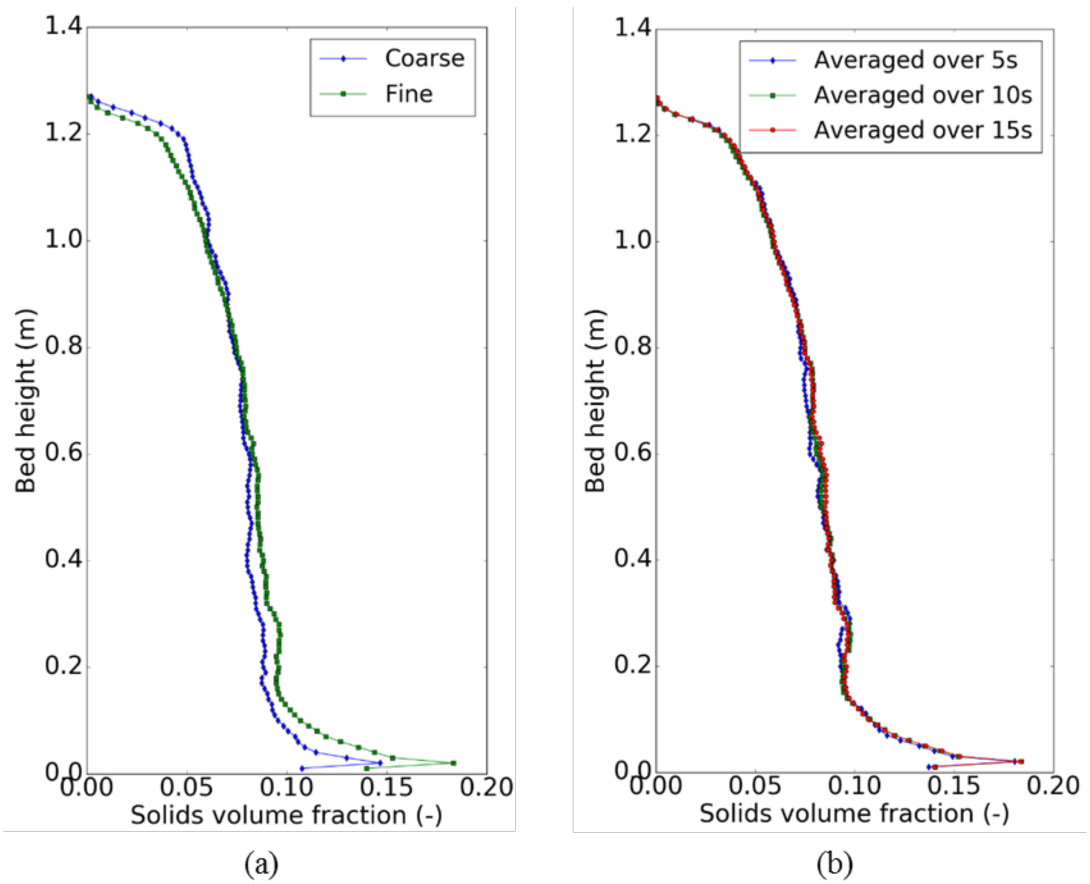


**Figure 2: Average solids holdup along the riser (simulated data were taken from the center line across the riser) (a) Systems with different grid resolutions; (b) systems with different statistical time.**

# 3. OBSERVATIONS

## 3.1 Evaluation of different drag models

Various drag models, used to calculate the drag coefficient, β, have been suggested in literature. One of the earliest correlations for drag coefficient is based on Wen and Yu's (Wen and Yu, 1966) work for predicting minimum fluidization velocity. The Gidaspow (Ding and Gidaspow, 1990) drag coefficient is a combination of Wen and Yu's correlation and Ergun's (S. Ergun, 1952) correlation derived from experiments on fluidized beds and packed columns. However, Wang et al. (Wang et al., 2008) reported that the Wen and Yu correlation is only reliable when particles are homogeneously dispersed within a control volume.

In recent years, drag correlations derived from DNS, such as Beetstra, Van der Hoef and Kuipers (BVK) (Beetstra et al., 2007) and Hill-Koch-Ladd (HKL) (HILL et al., 2001) have become more popular. BVK and HKL models were developed using Lattice-Boltzmann simulations in an effort to remove the need for empirical drag relations; instead, they use Reynolds numbers and packing fraction to control numerical predictions. However, these drag models are only valid for moderate Reynolds number flows, e.g., up to Re = 1000.

There is no consensus on the performance of the above drag models as related to a CFB full loop model. Most published results include the simulation of the CFB riser or bubbling bed only, and exclude the recirculation system. As such, this work examines BVK (Beetstra et al., 2007), Gidaspow (Ding and Gidaspow, 1990), Hill-Koch-Ladd (HILL et al., 2001), and Wen and Yu (Wen and Yu, 1966) by comparing computational results of the CFB full loop model with experimental data.

### 3.1.1 Pressure drop

From a practical perspective, the pressure profile of the CFB reflects the momentum exchange between gas and solids at specific operating conditions. In turn, the pressure profile mirrors the overall solids loading efficiency of the CFB as a system, and plays an important role in its design. Experimentally, matching a particular solids loading with a specific pressure profile results in reproducible hydrodynamics in a CFB riser (Berruti et al., 1995). Numerically, matching a particular solids loading with a specific pressure profile serves as model calibration. If a pressure profile cannot be reproduced numerically, the correction often lays in the selection of a more appropriate drag correlation.

Figure 3 shows the time averaged pressure profile of the CFB loop predicted with four different drag models. The figure illustrates that pressure profiles developed can be classified into two groups. Group 1 includes the empirical models: Wen & Yu and Gidaspow. Group 2 includes the DNS models: BVK and HKL. At low solids concentration, the Gidaspow model becomes the Wen & Yu model, so the similarity in low concentration regions is expected; however, some differences exist in dense regions, e.g., in the standpipe, the L-valve and the lower half of the riser. On the other hand, the largest differences between the Group 2 models are observed at the top of the riser. The difference between the Group 1 and 2 drag correlations is most obvious outside of the cyclone.

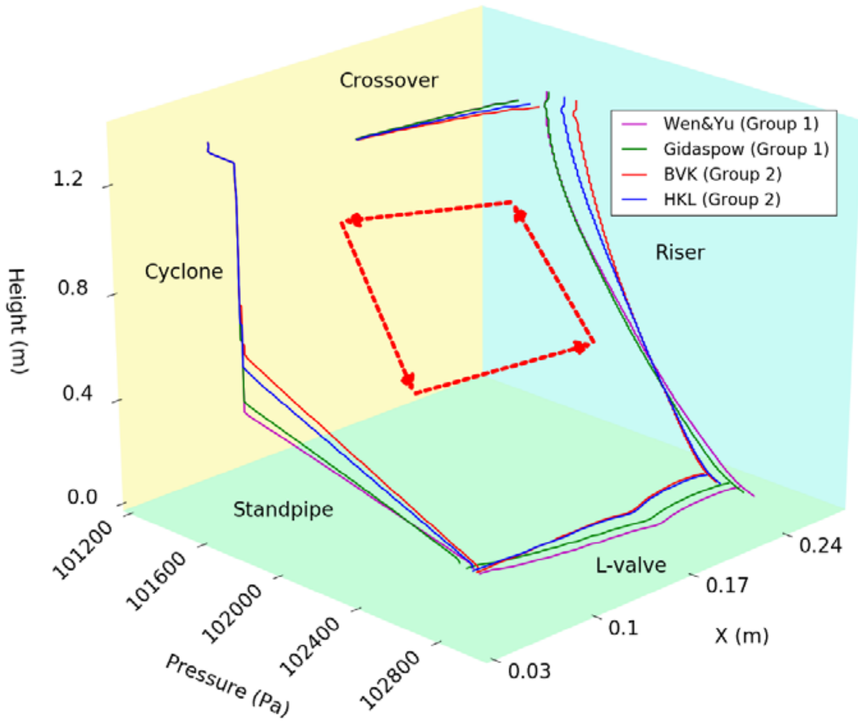


**Figure 3: Predicted, time-averaged pressure profile around the CFB system, the red arrows indicate the flow direction inside the CFB.**

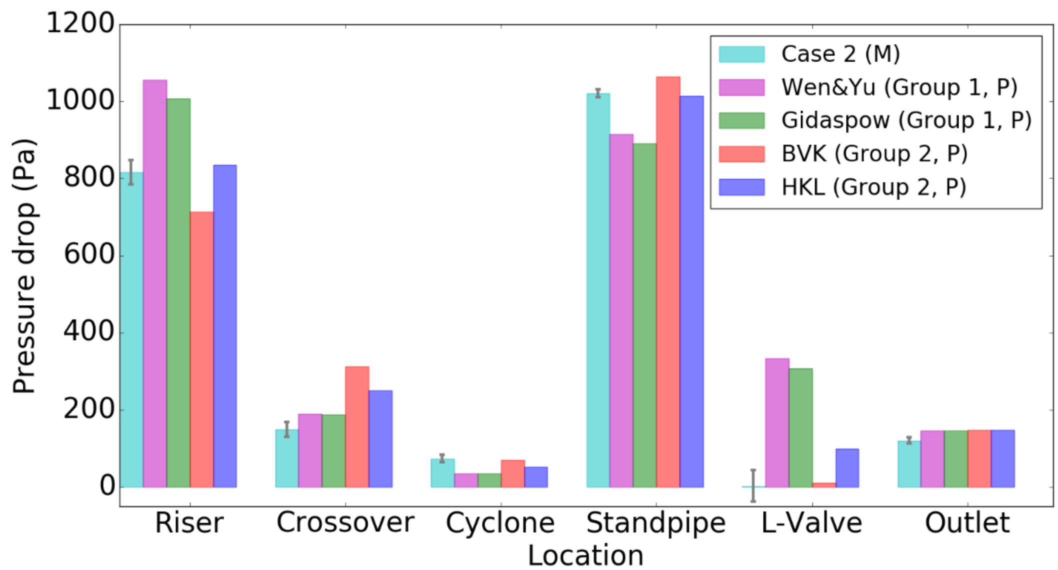


**Figure 4: Comparison of measured and predicted time-averaged pressure drop across key system components, the error bars represent the standard deviation between different measurements (M: Measured, P: Predicted).**

Figure 4 clarifies the pressure drop across key CFB system components identified in the pressure profiles of Figure 3. Additionally, two experimental case data sets are shown for comparison. As the figure reveals, the physical experiments are very reproducible run to run. Also, Figure 4 highlights that the Group 1 and Group 2 designates trend well together as general classes of drag correlations. Note that overall, the Group 2 models do a better job predicting component-ways and total system pressure drop.

### 3.1.2 Solids circulation rate

Solids circulation rate is another critical design and operational parameter in a CFB reactor system. However, only rarely is its numerical behavior studied, particularly in a full-loop system and at the particle level. Typically, circulation rate is set as an input boundary value for simulations that focus only on riser performance. Although a riser-only simulation provides a reasonable prediction of steady CFB riser flow, as Li et al. (Li et al., 2014) have pointed out, the questions remain: How well can a numerical model predict bed circulation rate on its own? i.e., when circulation rate is not prescribed as a boundary condition? Furthermore, what is the influence of different drag correlations on the predicted circulation rate? The full loop CFB simulations presented here explore such questions.

In the physical experiments, circulation rate is measured by analyzing the solids flow behavior with PIV at a detection window between the standpipe and the cyclone as illustrated in Figure 1 (b). High resolution images are recorded enabling a direct count of the particles via image analysis. The camera frame rate was set high enough to detect the highest particle velocities occurring in each riser. Low solid fluxes were measured by directly counting the number of particles that crossed a section of standpipe within a set time. Higher solid fluxes were calculated from measured velocity and estimated concentration using the high-speed video from HsPIV and an in-house calibration procedure (Panday et al., 2017).

In the numerical simulation, circulation rate is calculated by

$$G_s = V_d \rho_p (1 - \epsilon_g) A \tag{16}$$

where $V_d$ is the average descending velocity of solid mass, $\rho_p(1 - \epsilon_g)$ is the bulk density of solid mass and $A$ is the cross-sectional area of the detection window.

Figure 5 shows the predicted solids circulation rate derived under different drag correlations. The experimental measurements from operation condition 2 are used for reference. Using the drag correlation designates of Group 1 and Group 2 as before, the data presented in Table 3 make clear that the Group 1 drag correlations predict a lower solids circulation rate than Group 2.

**Table 3: Observed experimental and predicted mean solids circulation rates**

| | | Circulation Rate (g/s) |
|---|---|---|
| Experiment | | 6.8 +/- 1.5 |
| Group 1 | Wen&Yu | 2.99 +/- 2.42 |
| | Gidaspow | 2.17 +/- 1.93 |
| Group 2 | BVK | 16.9 +/- 4.14 |
| | HKL | 10.38 +/- 4.76 |

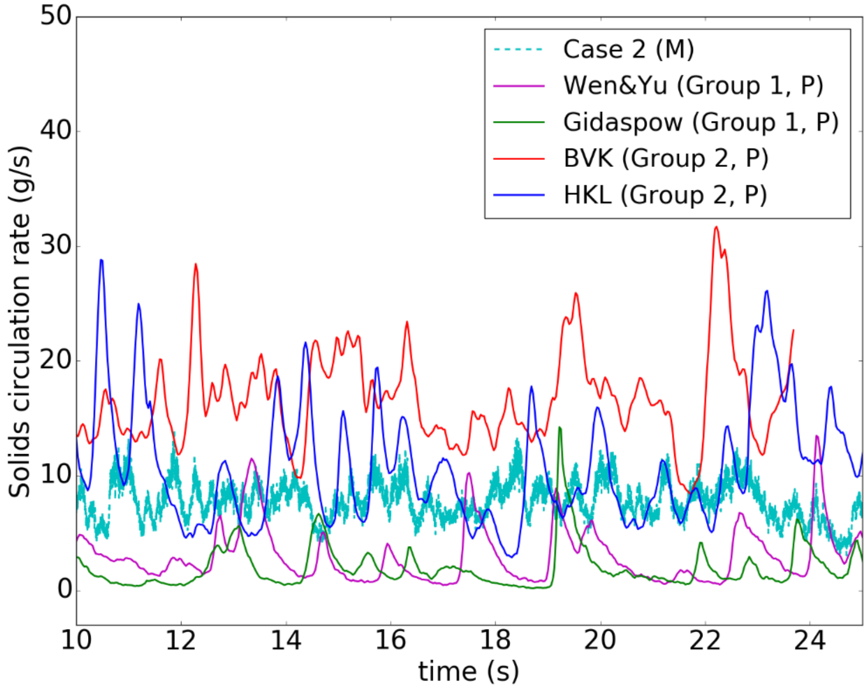


**Figure 5: Solids circulation rate predicted by different drag correlations (M: Measured, P: Predicted).**

### 3.1.3 Solids standpipe inventory height

Solids standpipe inventory height is an explicitly measurable comparison parameter. Particles temporarily accumulate in the standpipe after they leave the cyclone. Then, a pressure difference between the standpipe and riser causes the particles to return to the riser and begin another circuit through the CFB. Thus, solids standpipe inventory height is related directly to pressure differential and solids circulation rate.

The experimental apparatus is made from clear acrylic materials and the bed height inside the standpipe can be examined with a camera focused on the bed surface along with a ruler mounted outside the setup for clear measurement (Panday et al., 2017). To determine bed height from a simulation, the fluidized bed was divided into 1mm wide horizontal sections. In each section, solids volume fraction was calculated locally. Subsequently, bed height was delineated at the vertical level where the solids volume fraction changed abruptly from dense to dilute.

Figure 6 shows the predicted solids standpipe inventory height derived under different drag correlations. The experimental measurements from operation condition 2 are used for reference. Using the drag correlation designates of Group 1 and Group 2 as before, the data in Table 4 make clear that the Group 1 drag correlations predict a smaller solids standpipe inventory height than Group 2.

**Table 4: Observed experimental and predicted mean solids standpipe inventory height**

| | | Solids standpipe inventory height (m) |
|---|---|---|
| Experiment | | 0.47 +/- 0.02 |
| Group 1 | Wen & Yu | 0.36 +/- 0.01 |
| | Gidaspow | 0.39 +/- 0.01 |
| Group 2 | BVK | 0.57 +/- 0.01 |
| | HKL | 0.50 +/- 0.02 |

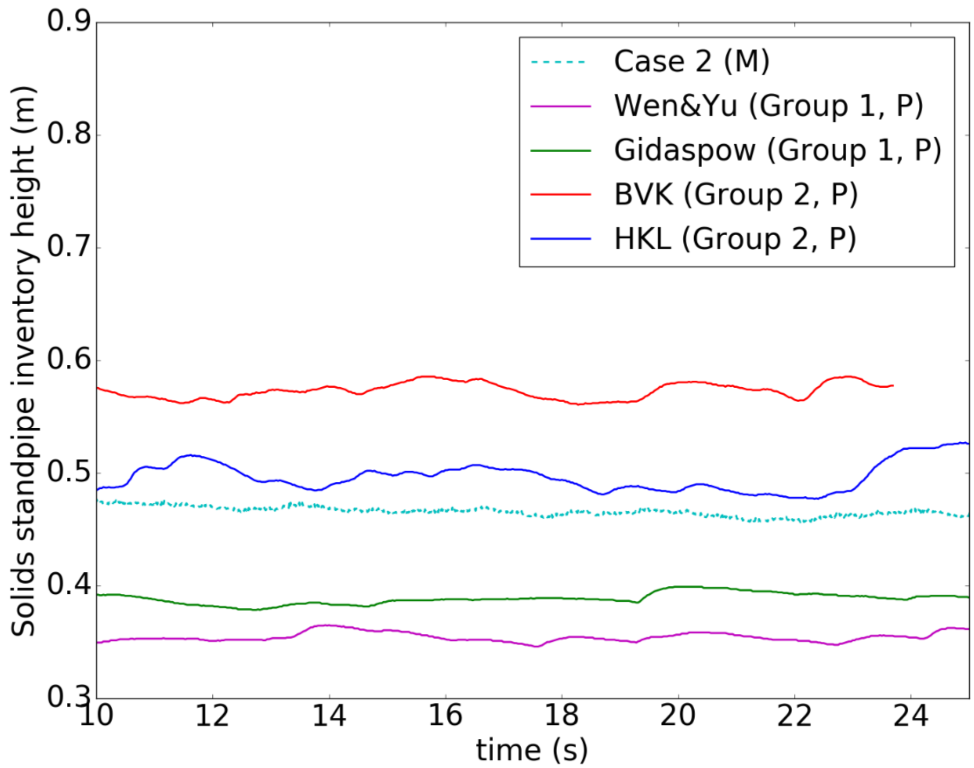


**Figure 6: Instantaneous solids standpipe inventory height under different drag correlations (M: Measured, P: Predicted).**

Figure 6 and Table 4 show that the HKL drag coefficient model offers the best agreement between experimental measurement and numerical prediction of solids standpipe inventory height.

### 3.1.4 Solid distribution inside the riser

An "S-shape" axial profile of solids volume fraction along the CFB riser has been shown under various flow conditions in different riser systems (Li et al., 1988; Louge and Chang, 1990). The profile is made of three distinct regions: (i) a dense bottom region, (ii) a dilute top section, and (iii) a middle section presenting a transition between (i) and (ii). With numerical simulations, the particle concentration along the profile can be estimated, and an evaluation of this documented physical phenomenon examined.

Figure 7 presents solids volume fraction along the center line of the CFB system as predicted by models utilizing the drag correlations in Groups 1 and 2. Note the very clear distinction between the two groups predictions, specifically in the riser. The solids volume fraction or in this context what would be called *the solids holdup,* is the primary cause of the pressure drop. Consequently, the higher solids volume fraction of Group 1 corresponds well with the recorded higher pressure drop discussed in Section 3.1.1.

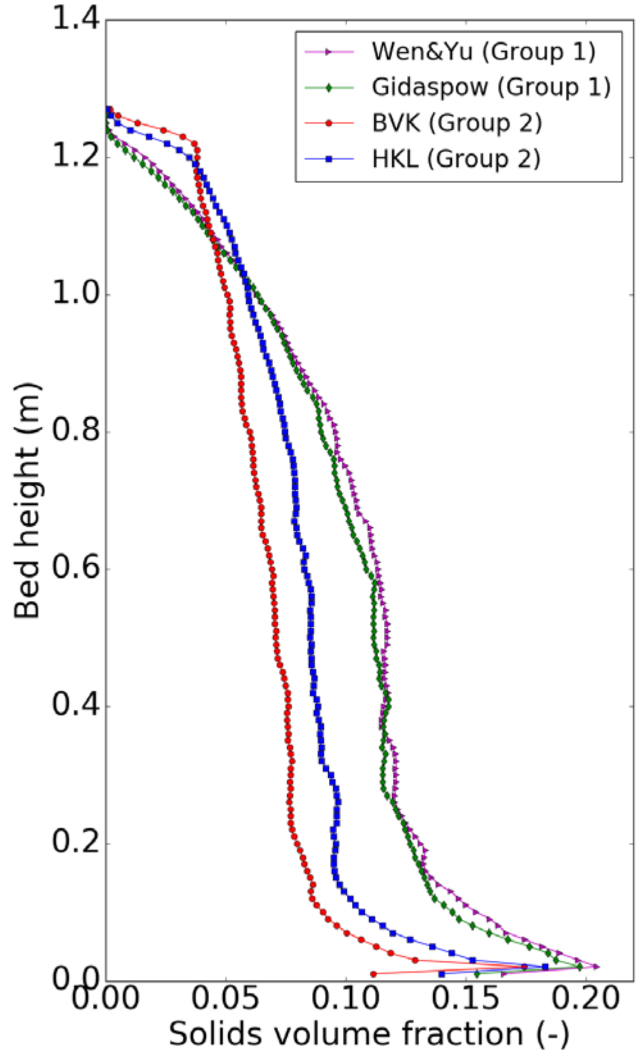


**Figure 7: Predicted solids volume fraction in the riser of the CFB system.**

Figure 8 illustrates time-averaged gas volume fraction along the longitudinal cross-section of the riser for each drag correlation. Note the similarity of Group 1 predictions, as well as those of Group 2 predictions. Recall that higher gas volume fraction indicates lower solids volume fraction. As such, the Group 1 predictions show more solids in the bottom of the riser, and an overall more striated solids pattern, whereas the Group 2 predictions show a more evenly distributed solids fraction, indicative of better fluidization along the length of the riser.

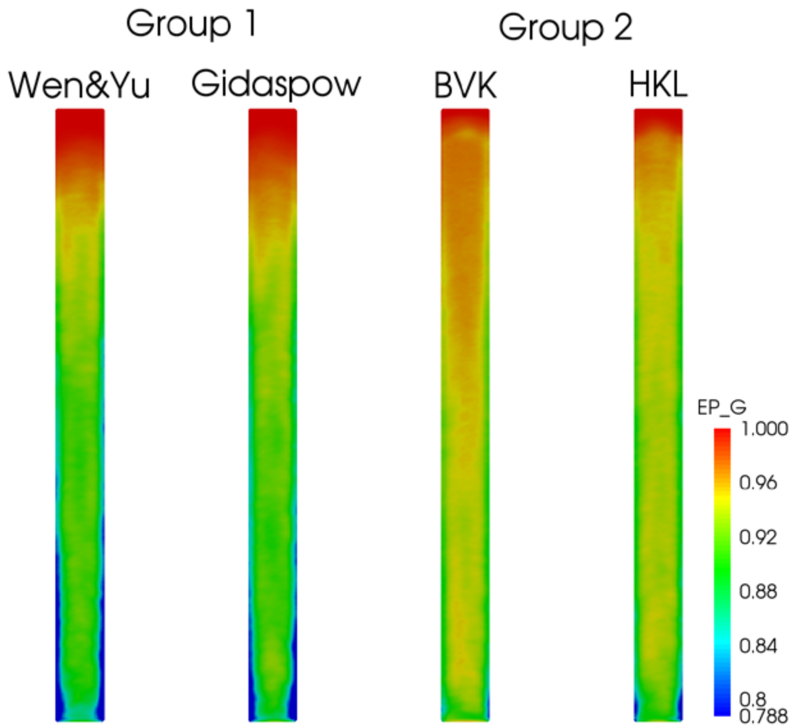


**Figure 8: Time-averaged gas void fraction along longitudinal cross section of riser under different drag correlations as labeled (the height of riser is scaled down for better representation)**

### 3.1.5 Core-annulus structure in the riser

A core-annulus structure usually refers to any flow that maintains a bulls-eye shape in cross-section, either through an evaluation of volume fraction or velocity. In the riser, the center-most region (or *core*) is characterized by a lower volume fraction and higher velocity of the solids phase. Here the solids are carried upward due to a relatively high gas flow. Along the wall of the riser, a lower velocity region, potentially even in downward flow, exhibits high solids concentration and represents the *annulus*. As a numerical example, using the HKL drag correlation, Figure 9 exhibits the average vertical particle velocity at different elevations along the riser. Note that particle velocity in the “core” is higher than near the wall; in fact, in some areas of the annulus, there are small regions of countercurrent (downward) flow.

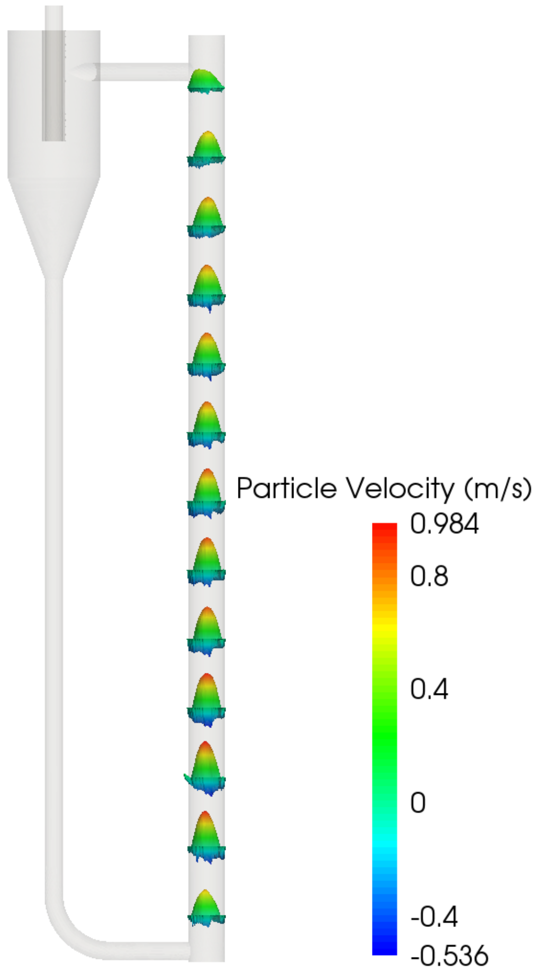


**Figure 9: The typical core-annulus structure (the average vertical particle velocity) along the riser with the HKL drag correlation.**

Figure 10 shows the average radial distribution of the solids volume fraction using different drag models. The "Core-Annulus" structure is captured by all four drag correlations tested. Yet again, there is a distinction between Group 1 and Group 2 models. Group 1 models predict higher solids holdup inside the riser. Group 2 shows a lower solids volume fraction in general, with a distinction between the results generated with BVK and HKL drag correlations.

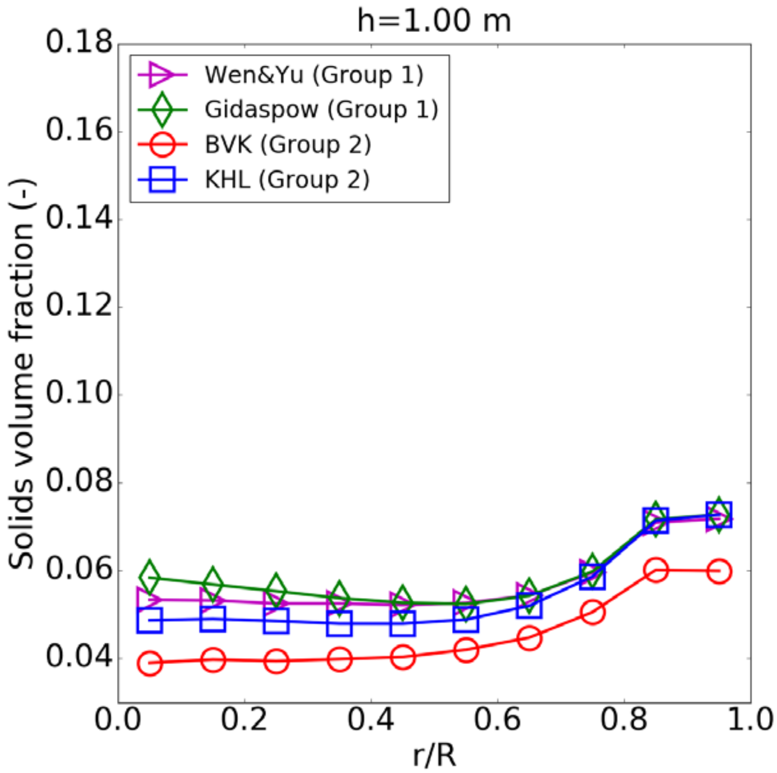
h=1.00 m
Wen&Yu (Group 1)
Gidaspow (Group 1)
BVK (Group 2)
KHL (Group 2)
Solids volume fraction (-)
0.18
0.16
0.14
0.12
0.10
0.08
0.06
0.04
0.0
0.2
0.4
0.6
0.8
1.0
r/R

**(a)**

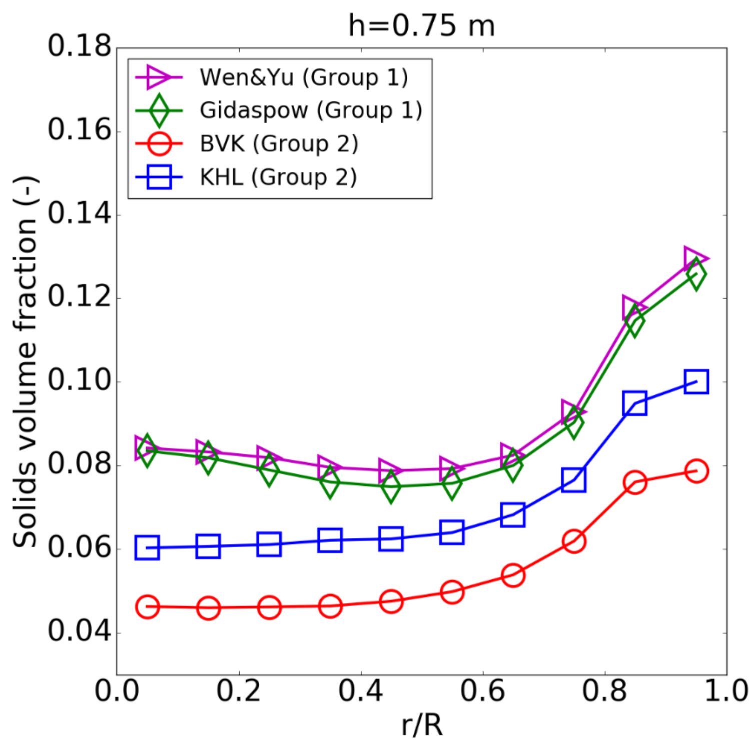
h=0.75 m
Wen&Yu (Group 1)
Gidaspow (Group 1)
BVK (Group 2)
KHL (Group 2)
Solids volume fraction (-)
0.18
0.16
0.14
0.12
0.10
0.08
0.06
0.04
0.0
0.2
0.4
0.6
0.8
1.0
r/R

**(b)**

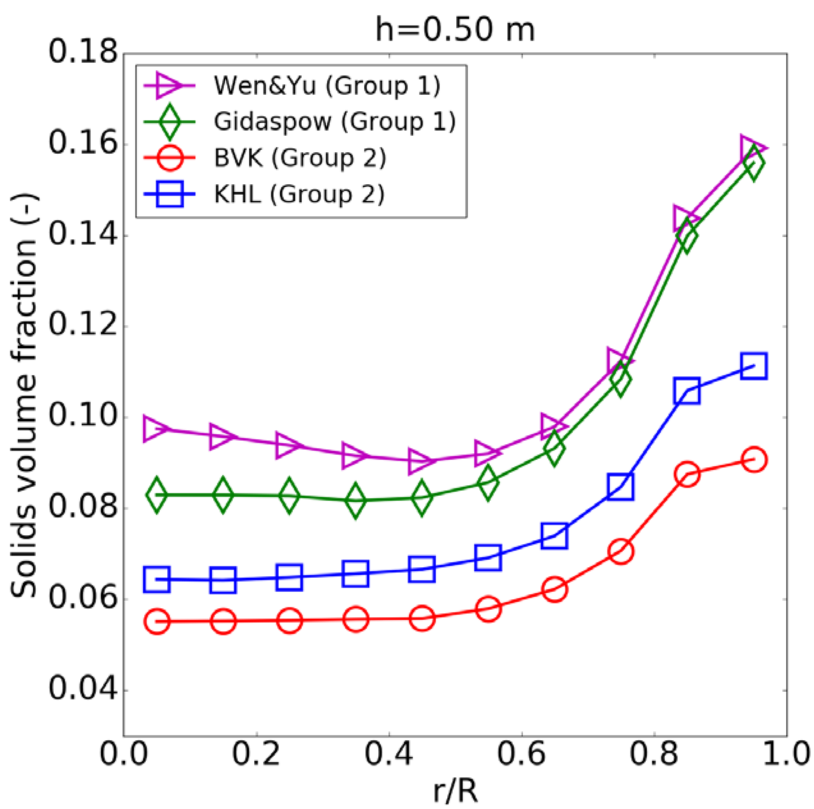
h=0.50 m
Wen&Yu (Group 1)
Gidaspow (Group 1)
BVK (Group 2)
KHL (Group 2)
Solids volume fraction (-)
r/R
0.18
0.16
0.14
0.12
0.10
0.08
0.06
0.04
0.0
0.2
0.4
0.6
0.8
1.0

**(c)**

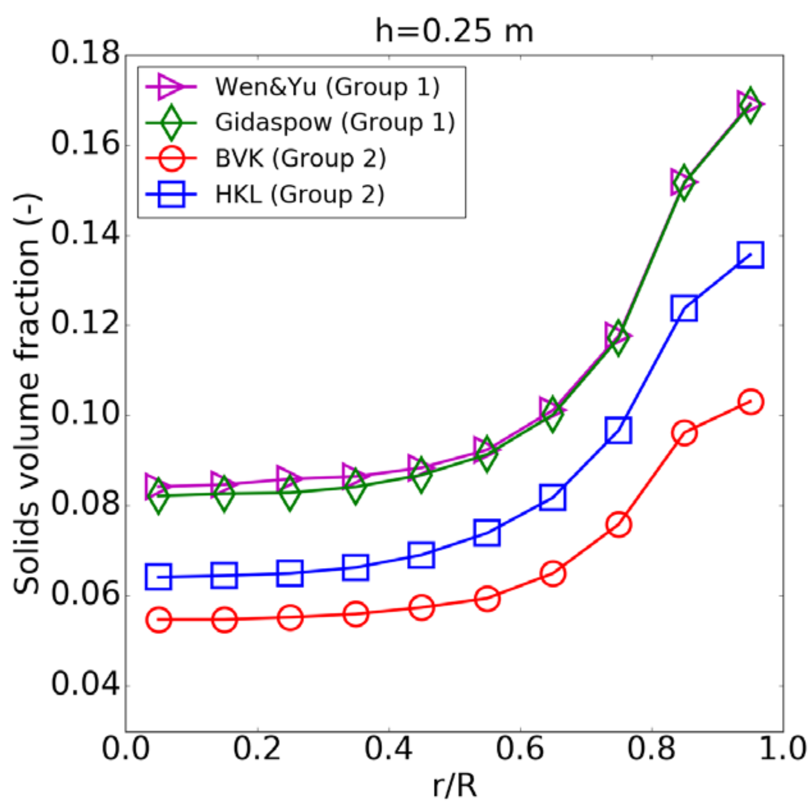
h=0.25 m
Wen&Yu (Group 1)
Gidaspow (Group 1)
BVK (Group 2)
HKL (Group 2)
Solids volume fraction (-)
r/R
0.18
0.16
0.14
0.12
0.10
0.08
0.06
0.04
0.0
0.2
0.4
0.6
0.8
1.0

**(d)**

**Figure 10: The average radial solids volume fraction at 4 different heights (a) 0.25 m, (b) 0.50 m, (c) 0.75 m, (d) 1.00 m. Note R is the radius of the riser and r/R is the dimensionless radial direction**

### 3.1.6 Residence time distribution

As the name indicates, particles circulate through the components of a CFB (riser, cyclone, standpipe). However, depending on which drag correlation is chosen, the flow behavior of individual solid particles through the different components results in different local residence times. It is known that particle distribution influences flow pattern and mixing behavior in the solid phase. Therefore, a better understanding of these residence times may help to improve the fluidizing process.

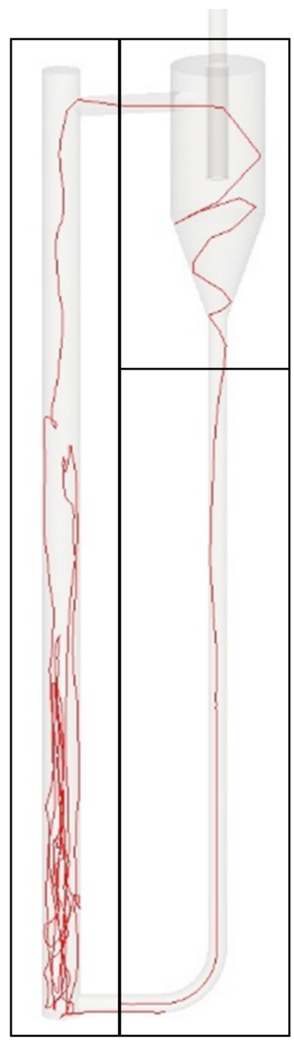

**Figure 11: Trajectory of a tracer particle inside the CFB and the division of the system for the calculation of the residence times.**

With CFD-DEM, it is straightforward to determine the residence time of the solids particles in each part of the CFB. Residence time is estimated by dividing the system into three different parts:

cyclone, standpipe and riser as shown in Figure11, along with a trajectory of a test particle making one full loop inside the CFB.

As can be seen in Figure 12, the residence time of the particles in the cyclone is quite short, and the distribution is narrow for different drag correlations. On the other hand, the residence time in the standpipe and riser are quite dissimilar for different drag laws. Group 2 drag correlations predict a larger drag force on the particles, resulting in a higher solids circulation rate and shorter residence time in both standpipe and riser. Group 1 drag models predict a smaller drag force, resulting in a lower solids circulation rate and longer residence time in both standpipe and riser. Moreover, the residence time distribution of Group 1 models is wider and flatter than the Group 2 predictions that show a clear peak and a long tail (which can be well fit with a log-normal distribution). This difference is caused by the fact that the solids circulation rate is very low in Group 1. Models with low circulation rates would require many hundreds of seconds of run-time to move all particles at least one loop cycle.

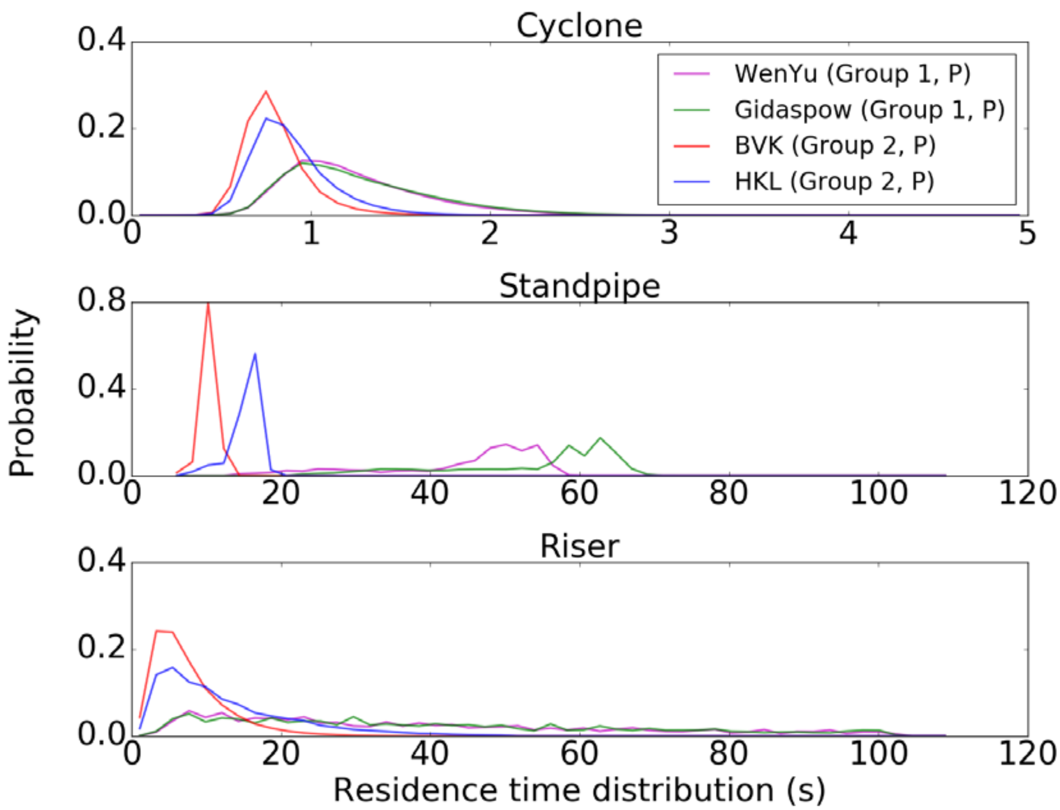


**Figure 12: Residence time distribution in different components of the CFB under different drag correlations**

### 3.2 Influence of the particle size distribution

Particle size distribution (PSD) is known to have a strong influence on the hydrodynamics and related characteristics of gas–solid fluidized beds (such as mixing and conversion). In most cases, mono-dispersity enhances bed stability, thus facilitating bed operation because de-fluidizing, segregation and entrainment are reduced. Note that in some cases a broad PSD is found to be advantageous for fluidization and chemical conversion, but these particular phenomena are not of interest in these experiments. Much experimental and numerical simulation work has been done to characterize flow behavior, such as minimum fluidization velocities, ranging through all Geldart particle classifications. In this work, both mono-disperse (narrow cut) particles and poly-disperse (broad cut) particle distributions are simulated and the results compared with each other.

First, particle size distribution is measured experimentally. Figure 13 shows these measured results, along with the values used in subsequent numerical simulations. Note that the difference between the distributions is caused by the existence of both very small and very large particles in a real distribution. Such values can skew numerical simulations unexpectedly, and are therefore removed from consideration.

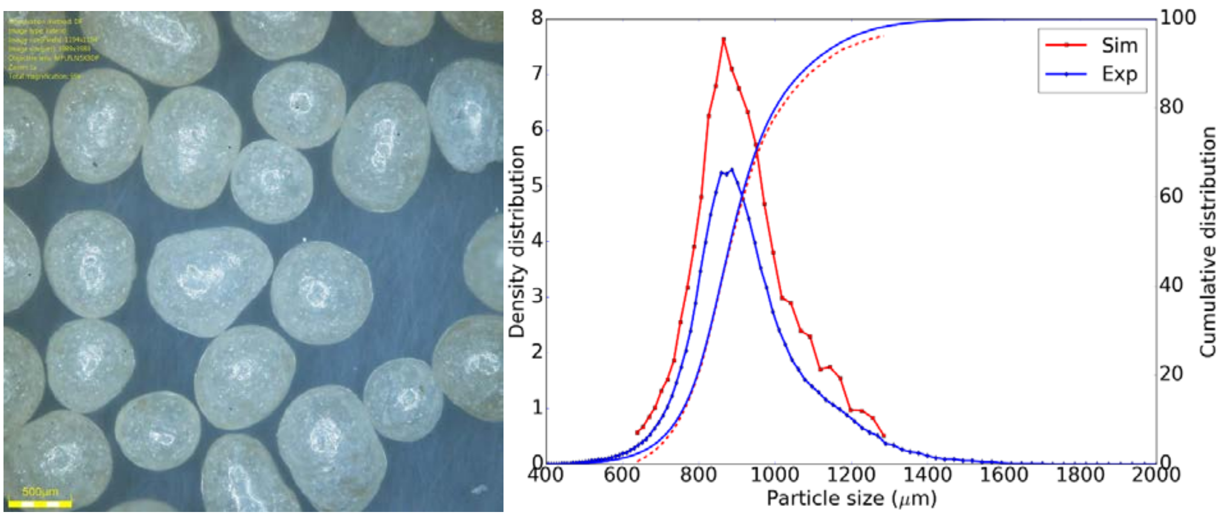


**Figure 13: Particle size distribution. Sim = used in simulation; Exp = measured values**

In the following sections, pressure drop, solids circulation rate and solids standpipe height are evaluated using this poly-disperse size distribution in cooperation with the HKL drag correlation. Recall that the earlier evaluations were completed on a mono-disperse cut, as defined in Table 2.

To seed the numerical simulations, a cubic lattice arrangement of small and large particles is created. This results in a more loose initial bed, but after a small transient, particle height in the standpipe inventory is similar to experimental set-ups.

### 3.2.1 Pressure drop

Figure 14 compares pressure drop between the different parts of the CFB as illustrated in Figure 1(b). Figure 14 includes the data associated with both mono-disperse and poly-disperse particles as well as corresponding experimental values. These data make clear that particle size distribution has minor effect on pressure drop across key system components.

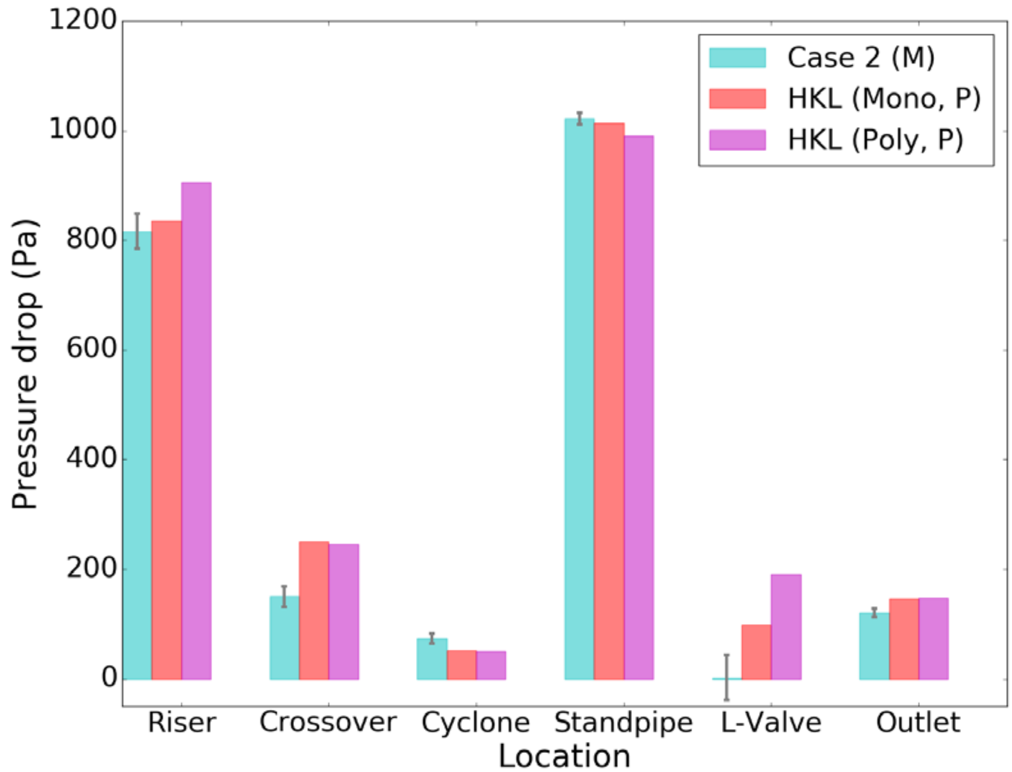


**Figure 14: Comparison of measured and predicted time-averaged pressure drop across key system components (M: Measured, P: Predicted, Mono: Mono-disperse, Poly: Poly-disperse).**

### 3.2.2 Solids circulation rate

Solids circulation rate was analyzed for both mono-disperse and poly-disperse particle size distributions. Figure 15 shows that both cases predict similar solids circulation rates with the average solids circulation rate of 9.32 and 8.80 g/s for mono-disperse and poly-disperse, respectively.

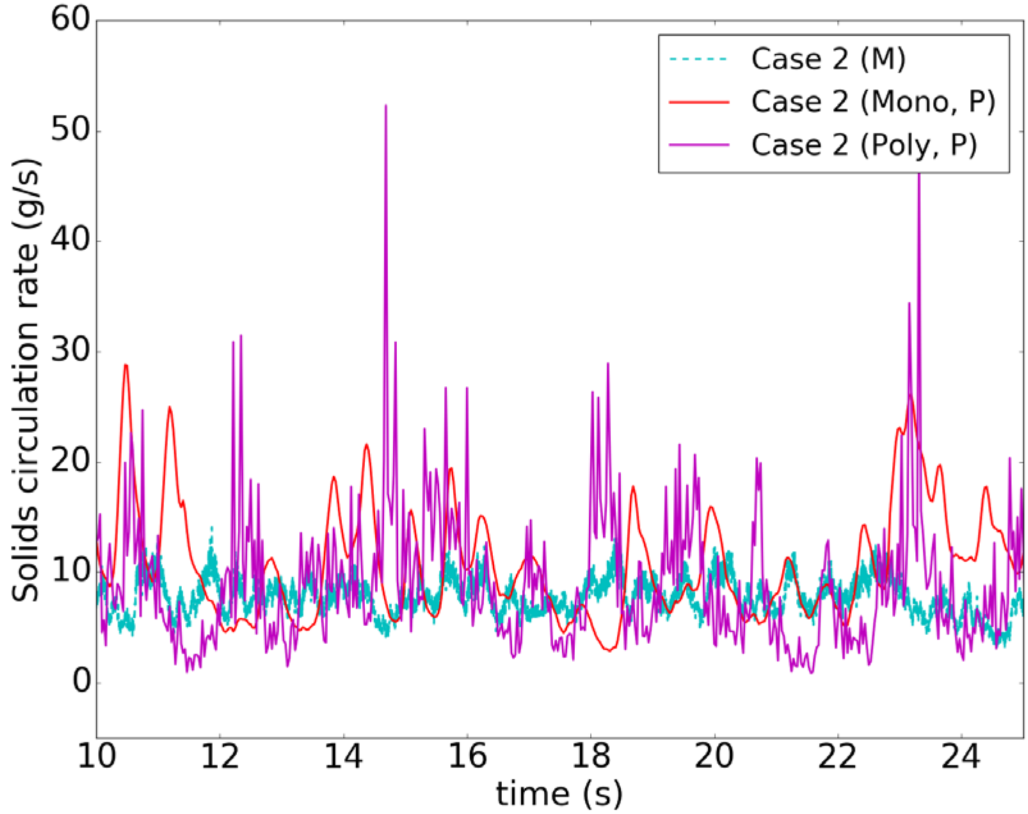


**Figure 15: Solids circulation rate with and without particle size distribution (M: Measured, P: Predicted, Mono: Mono-disperse, Poly: Poly-disperse).**

### 3.2.3 Solids standpipe inventory height

Additionally, solids standpipe inventory height is compared. Results are shown in Figure 16.

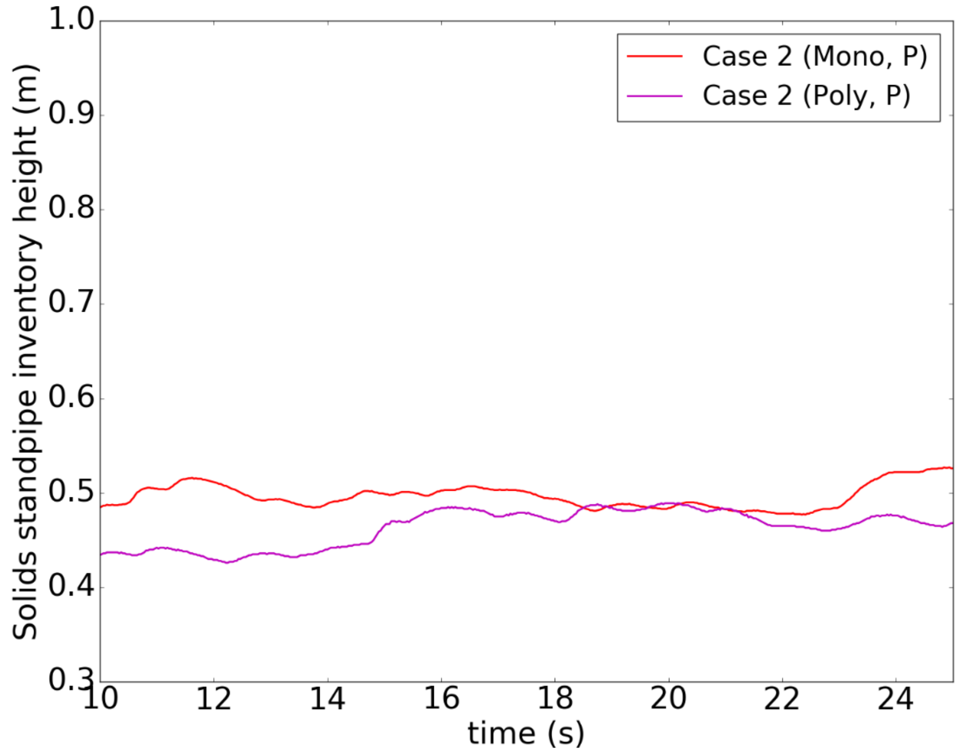


**Figure 16: Solids standpipe inventory height (P: Predicted, Mono: Mono-disperse, Poly: Poly-disperse).**

Based on the above comparison of pressure drop, solids circulation rate and solids standpipe inventory height between mono- and poly-disperse particle systems, it is clear that the influence of particle size distribution on flow hydrodynamic behavior in this CFB with these solids (HDEP) is small. Consequently, mono-disperse particles will be used for simulation results presented hereafter.

### 3.3 Further comparison under different operating conditions

The results presented in Section 3.1 were compared against experimental operating case 2 (as outlined in Table 2) to substantiate the CFD-DEM, and to assess four different drag correlations. Of these drag correlations, the HKL model appeared most reliable for numerical CFB simulation. In this section, two additional operating conditions are examined (defined as case 1 and case 3 in Table 2). Figure 17 offers a photograph of each experimental set-up in concert with its associated simulation, under 3 operating conditions.

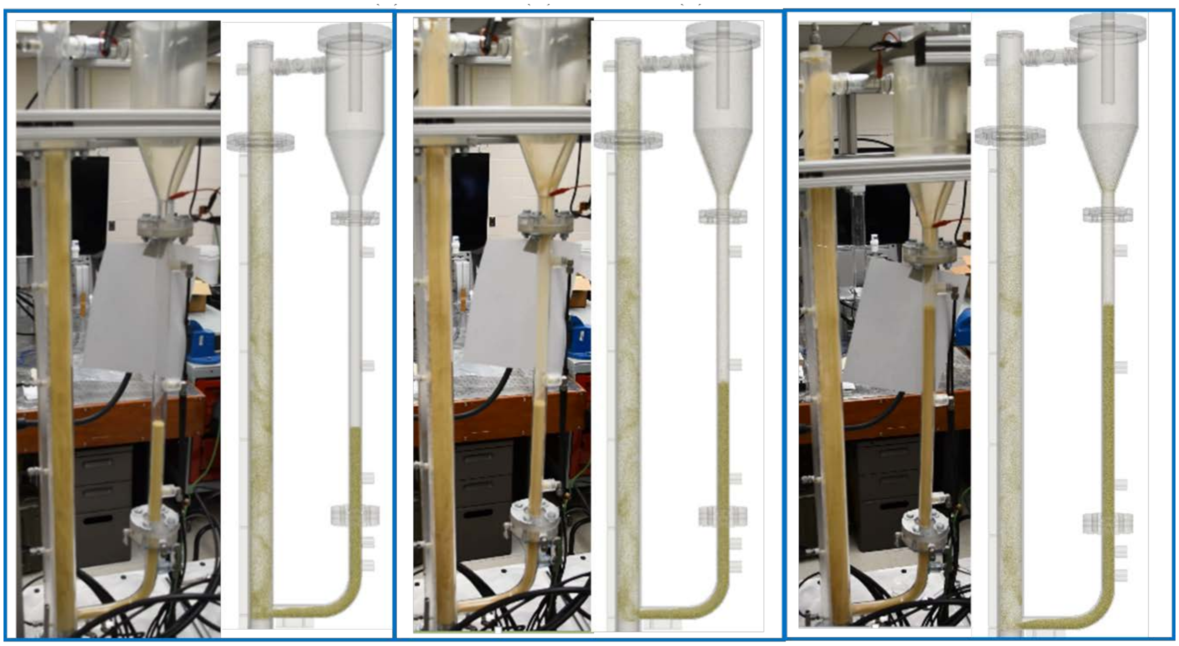

(a) (b) (c)

**Figure 17: Direct comparison between experiments and simulations under different operating conditions (a): Case 1, (b): Case 2, (c): Case 3.**

#### 3.3.1 Pressure drop

Pressure measurements provide a simple and practical means to estimate key hydrodynamic properties of gas-fluidized beds. For example, the maximum standard deviation of pressure fluctuations across a fluidized bed as a function of superficial gas velocity is accepted as an indicator of the transition from bubbling to a turbulent fluidization flow regime. This transition is caused by the break-up of bubbles or slugs into transient voids (Johnsson et al., 2000; Ellis et al., 2003). Likewise, axial pressure profiles along fluidized beds can indicate the hold-up of particles in different sections of the bed. For circulating fluidized beds, pressure measurements are used to determine solids inventory in the riser section; they can also indicate flow instabilities and disturbances in the cyclone and the standpipe by way of dynamic measurements of the pressure loop (Werther, 1999). A comparison of pressure drop within the experimental CFB, detailed by component, is presented in Figure 18. Each graph compares two experimental data sets measured at different times, along with predictions from an associated numerical simulation. There is decent matching between experimental and simulated data over all cases.

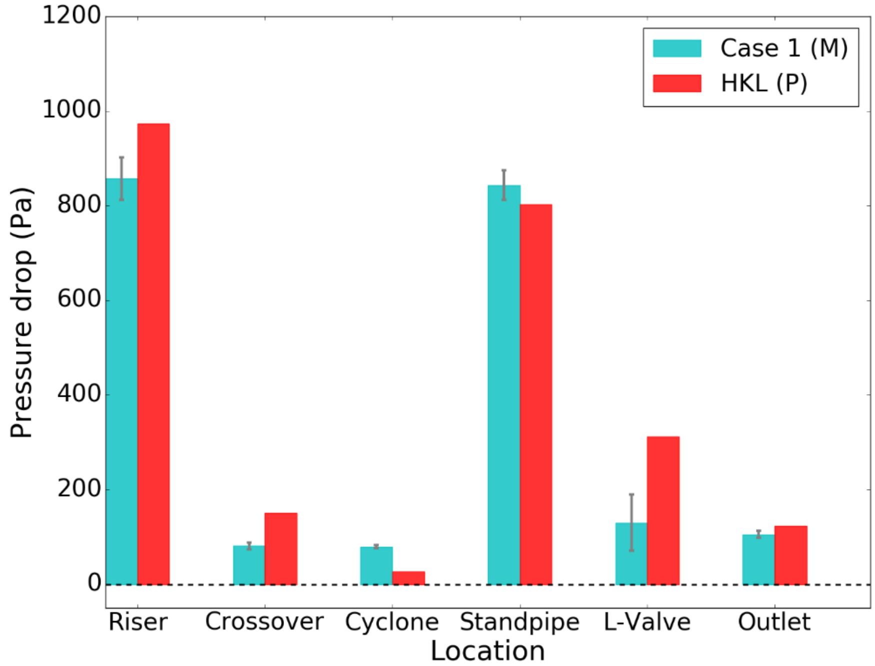


(a) Case 1

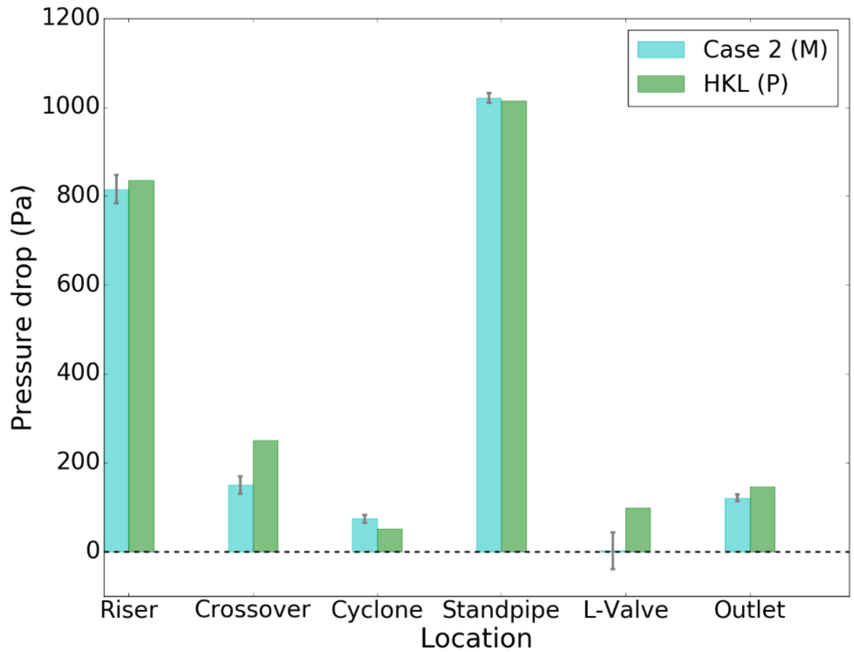


(b) Case 2

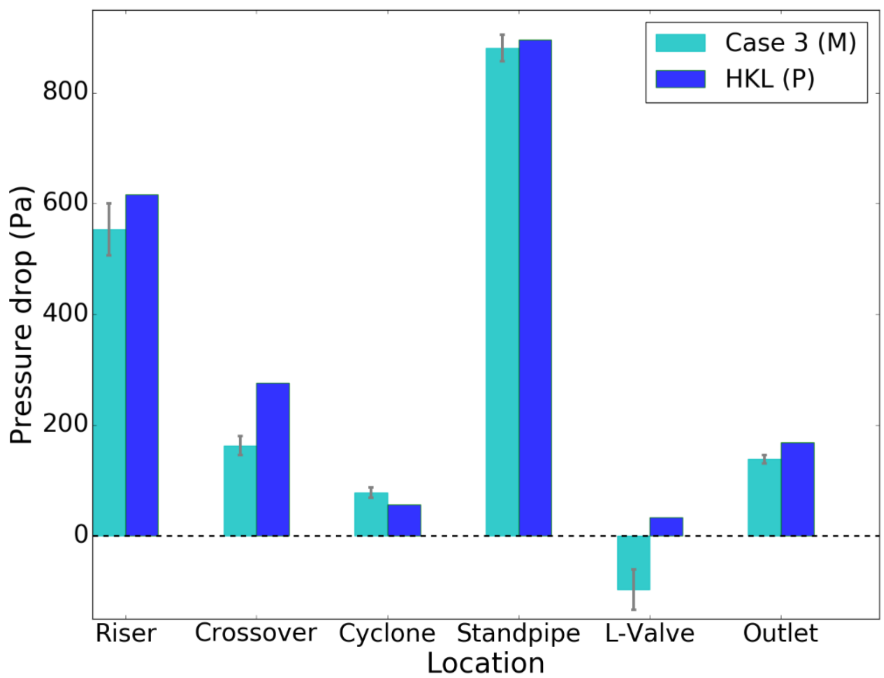


(c) Case 3

**Figure 18: Direct comparison of pressure drop at different locations under all 3 operation conditions.**

### 3.3.2 Solids circulation rate

**Table 5: Solids circulation rate**

| | | Experiment | Simulation |
|---|---|---|---|
| Solids circulation rate (g/s) | Case 1 | 0.06±0.1 | 0.36 +/- 0.37 |
| | Case 2 | 6.8±1.5 | 10.38 +/- 4.76 |
| | Case 3 | 7.9±1.5 | 10.66 +/- 4.09 |

A direct comparison of the average solids circulation rate under different operating conditions is listed in Table 5. Considered a critical design and operational parameter in a CFB reactor system, solids circulation rate is studied only rarely at the particle level. The table reveals that the predictions created by the HKL drag model are considerably higher than measured experimental observations under these operating conditions. This disparity warrants further study.

### 3.3.3 Solids standpipe inventory height

Figure 19 presents the experimentally measured solids standpipe inventory height compared to numerical prediction for all three experiments. Table 6 then compares the experimental and numerical time-averaged values for the same data sets. Note that the data match is quite good.

**Table 6: Standpipe bed height**

| | | Experiment | Simulation |
|---|---|---|---|
| Standpipe bed height (m) | Case 1 | 0.43 +/- 0.01 | 0.42 +/- 0.01 |
| | Case 2 | 0.47 +/- 0.01 | 0.50 +/- 0.02 |
| | Case 3 | 0.65 +/- 0.01 | 0.68 +/- 0.01 |

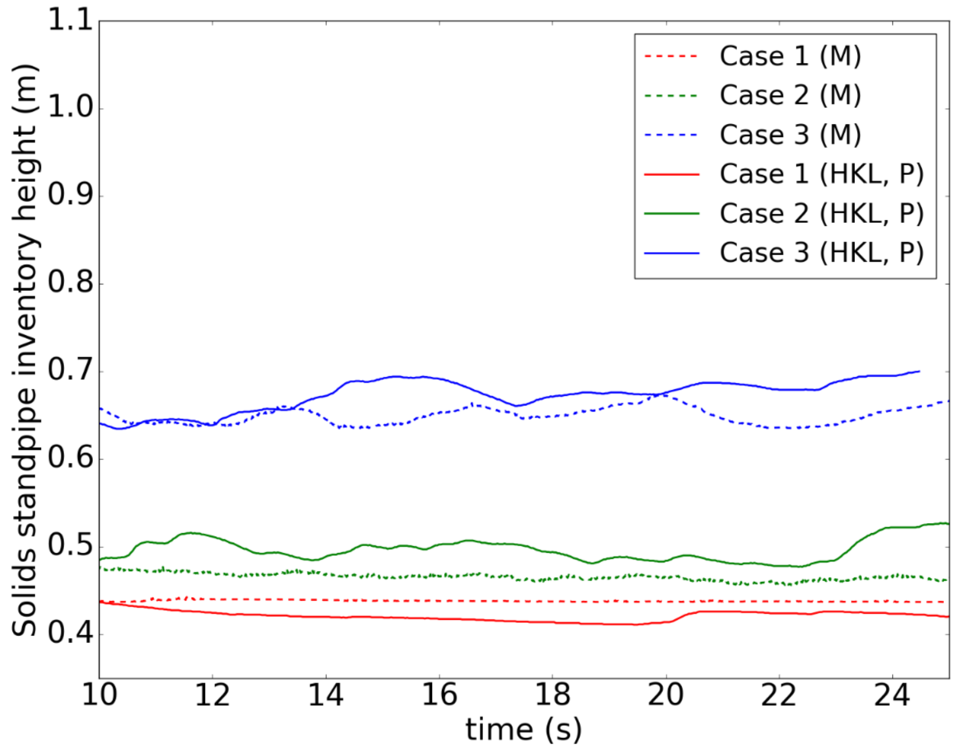


**Figure 19: Direct comparison of the solids standpipe inventory height under different operation conditions (M: Measured, P: Predicted).**

### 3.3.4 Solids volume fraction in the riser (S-shape)

An "S-shape" axial profile of solids volume fraction along the riser has been shown in different work, under various flow conditions and in different riser systems (Li et al., 1988; Louge and Chang, 1990). Likewise, using the numerical simulations presented in this report, solids volume fraction can be examined along the center line of the CFB's riser. Figure 20 presents the S-shape formed under the 3 operational conditions examined.

Interestingly, the radial distribution of the solids holdup are distinct under different operating conditions. In case 1, the axial profile is non-uniform with high solids concentration (solids holdup) near the solid inlet, then decreasing gradually upwards to the top of the riser and decreasing smoothly towards the outlet of the riser. In case 2, the axial profile is relatively uniform in the middle part of the riser with an average around 0.1%. The solids holdup near the inlet is higher than the middle part but decreases abruptly towards the outlet of the riser. Finally, the results of case 3 are quite similar to case 2, with even more uniform solid holdup in the middle part of the riser averaging about 0.07%.

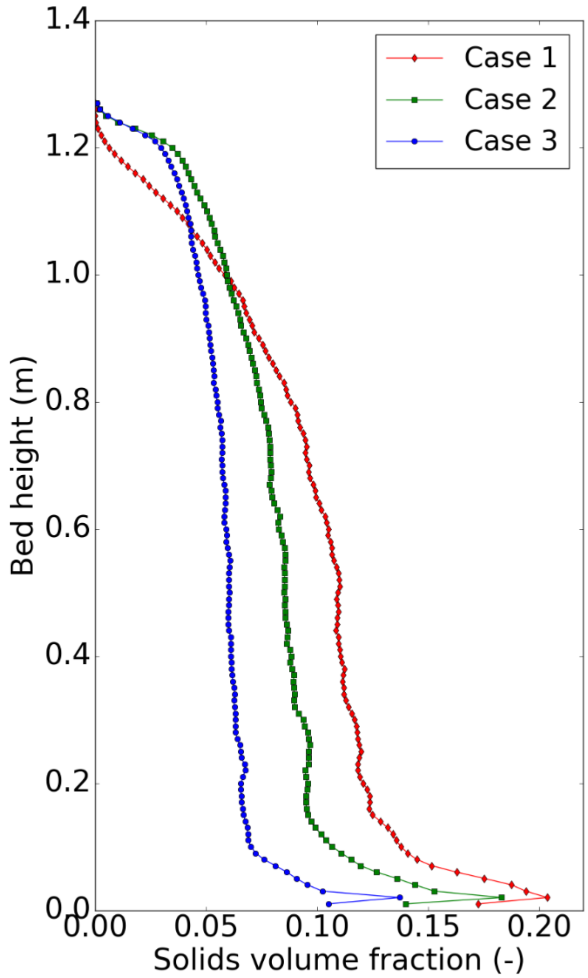


**Figure 20: Average solid holdup along the riser under different operation conditions.**

Figure 21 illustrates time-averaged gas volume fraction for the three operating conditions along the longitudinal cross-section of the riser. In concert with Figure 20, one can see clearly the uniform solids holdup in the middle of the riser for cases 2 and 3. One can also see the distinct core-annular structure of the flows. Most importantly, this visual representation makes more clear the cause of pressure drop, i.e. concentrated solids holdup, and how the structure of that solids holdup is influenced by operating conditions of the CFB.

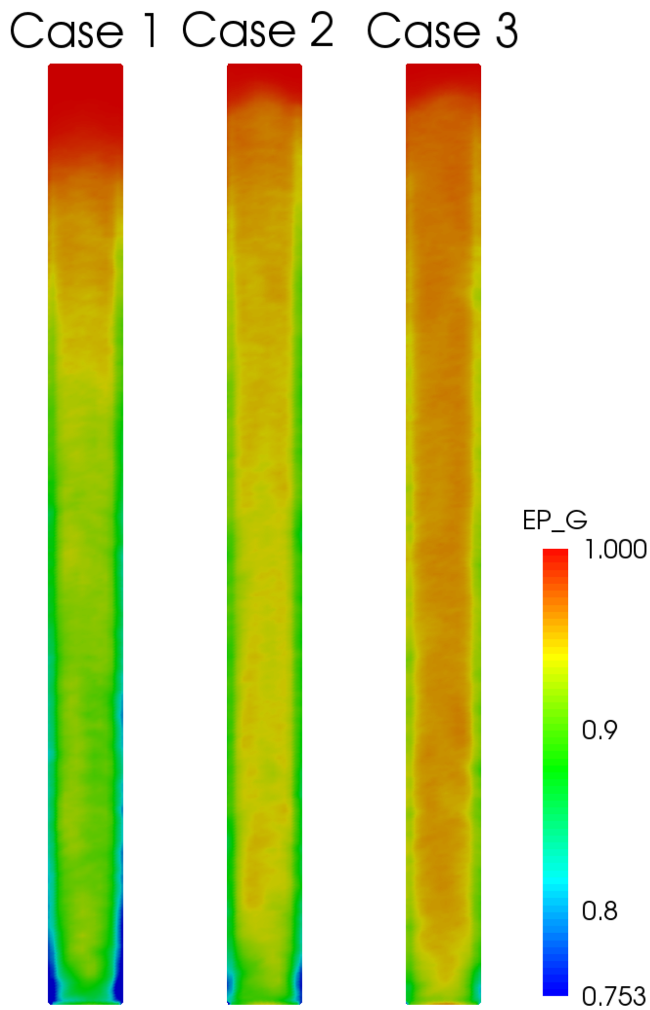


**Figure 21: Time-averaged gas void fraction of the center surface inside the riser under different drag correlations.**

### 3.3.5 Core Annulus structure inside the riser

Figure 22 presents radial cross-sectional views of solid axial velocity along the riser for 3 operating conditions. In particular, the cross sections are taken at 0.25 m, 0.50 m, 0.75 m and 1.00 m from the riser inlet.

Figure 23 shows the average radial solids volume fraction corresponding to the slices shown in Figure 22.

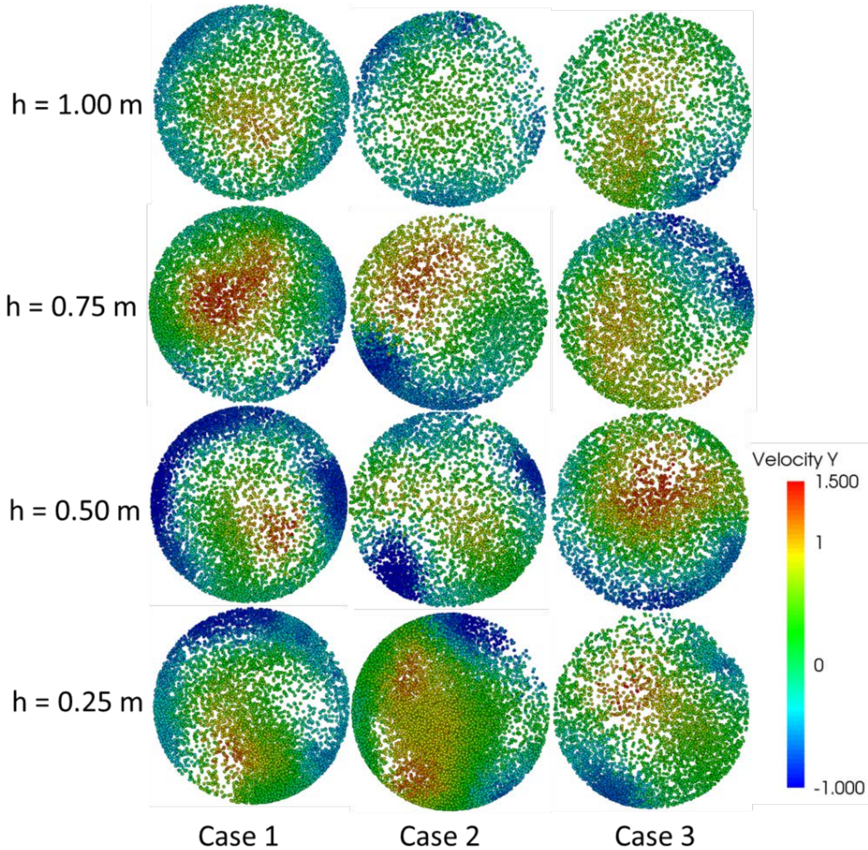


**Figure 22: Influence of different operating conditions on instantaneous solid velocity. Shown are radial cross sections of the CFB riser at indicated heights (h) from the inlet**

Figures 22 and 23 confirm the core-annular structure formed in the riser for all three operating cases. Furthermore, they better indicate the nature of solids hold-up in the riser as it relates specifically to solids velocity. It appears that lower solids velocity in the riser results in a build-up of solids near the inlet. Higher solids velocity tends to more evenly distribute solids through the riser.

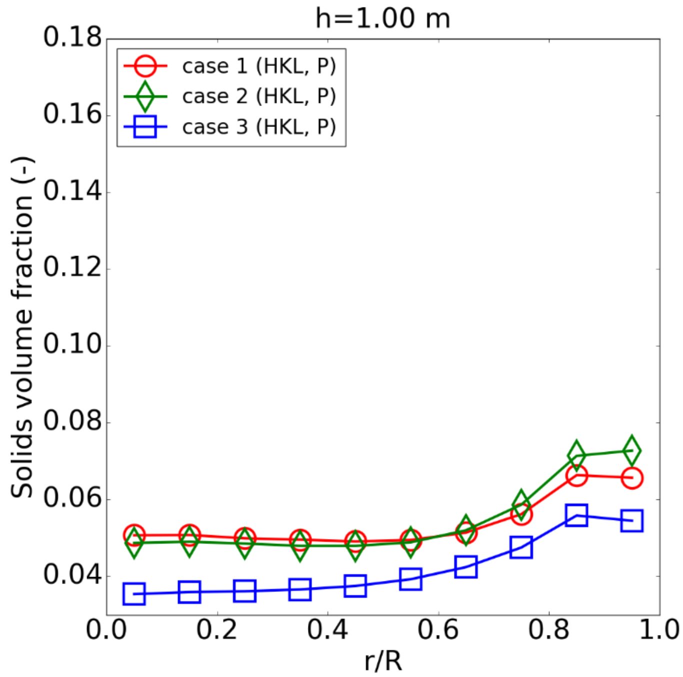
h=1.00 m
case 1 (HKL, P)
case 2 (HKL, P)
case 3 (HKL, P)
Solids volume fraction (-)
0.18
0.16
0.14
0.12
0.10
0.08
0.06
0.04
0.0
0.2
0.4
0.6
0.8
1.0
r/R

**(a)**

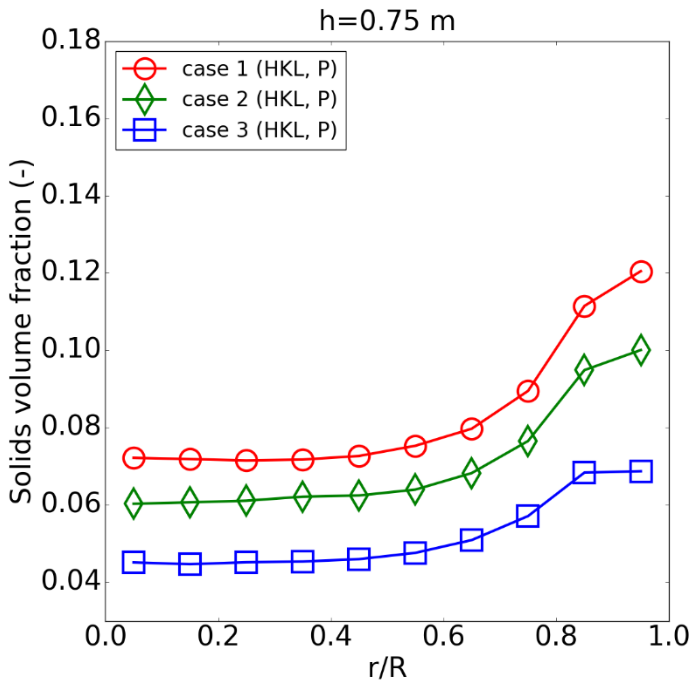
h=0.75 m
case 1 (HKL, P)
case 2 (HKL, P)
case 3 (HKL, P)
Solids volume fraction (-)
0.18
0.16
0.14
0.12
0.10
0.08
0.06
0.04
0.0
0.2
0.4
0.6
0.8
1.0
r/R

**(b)**

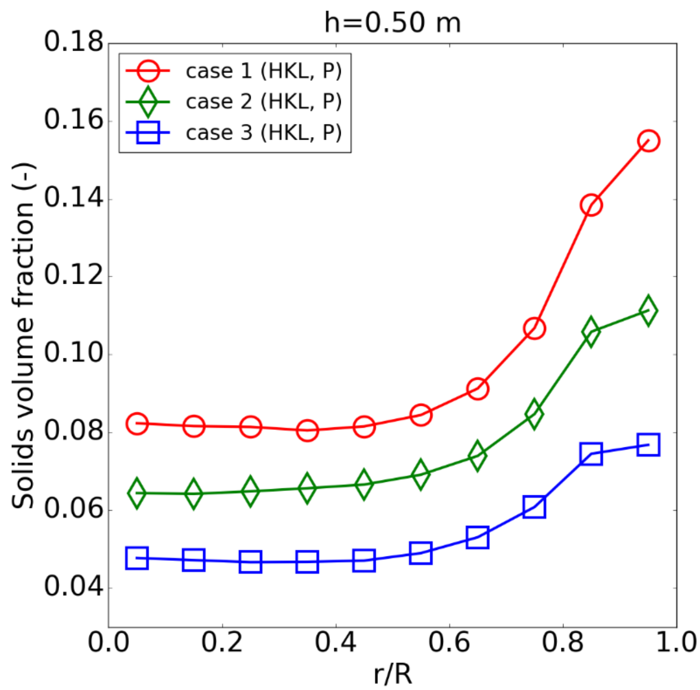


**(c)**

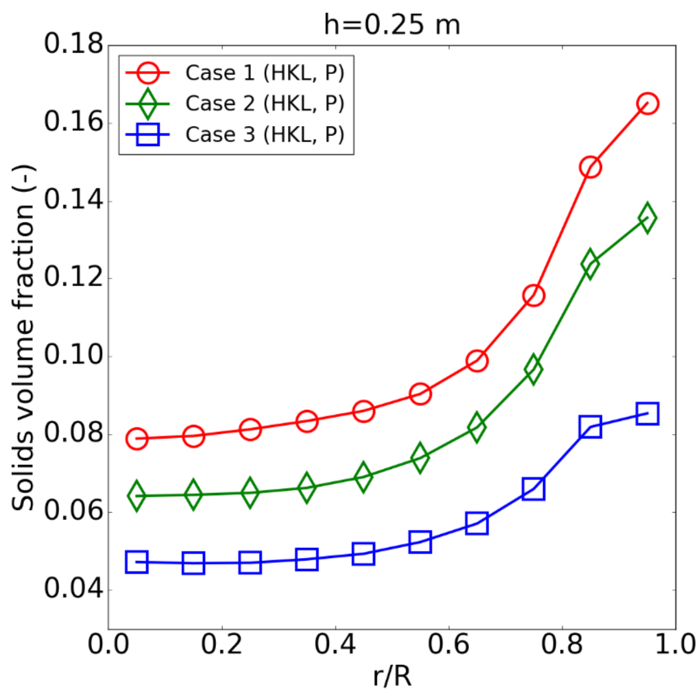


**(d)**

**Figure 23: The average radial solids volume fraction at 4 different heights (a) 1.00 m, (b) 0.75 m, (c) 0.50 m, (d) 0.25 m under 3 different operation conditions, here r/R is the dimensionless radial direction.**

### 3.3.6 Residence time distribution

Figure 24 presents the residence time for solids in three basic components of a CFB: the cyclone, the standpipe and the riser. As shown, Cases 2 and 3, which operate at the higher gas injection rates, are quite similar. The exception is in the standpipe, where residence time is more varied for Case 3, which is due to the less aeration gas introduced into the L-valve. Overall, Case 1 appears to suffer considerably from an under-blown bed.

Different operating conditions influence the flow behaviors of solid particles in these three components, and consequently affect the residence time for the solid phase as it moves through the system. Understanding the flow pattern and mixing behavior of the solid phase can be used to improve gas–solid interaction efficiency and production quality in fluidizing processes.

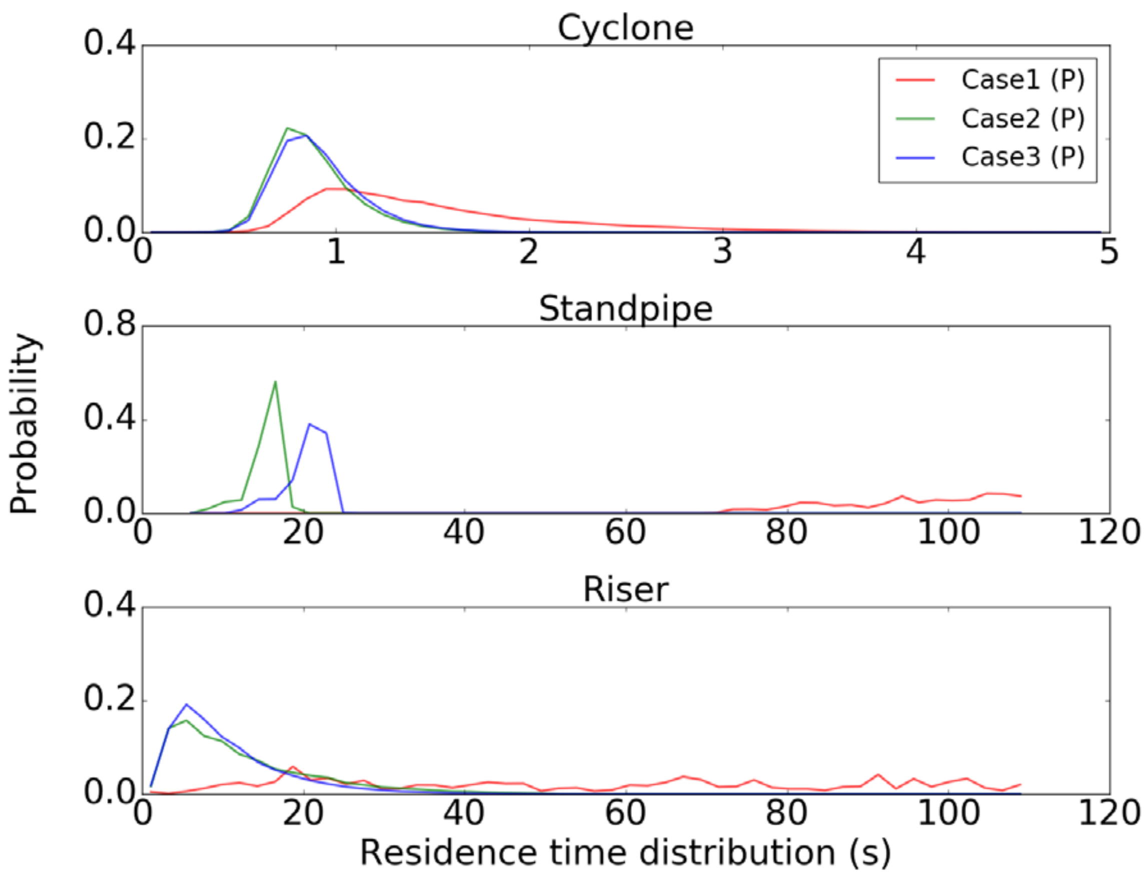


**Figure 24: Residence time distribution through different components of the CFB under 3 different operating conditions.**

## 4. CONCLUSIONS

Numerical CFD-DEM simulations of the hydrodynamic behavior of solid particles inside a lab-scale, full loop CFB were conducted with the U.S. Department of Energy's Multiphase Flow with Interphase eXchanges code, MFIX. Predictions from the simulations were compared directly with experimental measurements from a lab-scale CFB unit at NETL.

The novelty of this work relies on the simulation of the full-loop CFB operation in concert with a similarly scaled operating CFB unit. Most relevant published numerical works focus only on riser simulation.

Four drag correlation models were examined in the context of CFD-DEM. Comparative results indicated that the DNS-based Hill-Koch-Ladd model best predicted pressure drop and standpipe inventory height regardless of operational case. Solids circulation rate was not well-modeled by any drag correlation tested, and further investigation is needed to better understand this phenomenon.

The accuracy of pressure drop through the CFB and standpipe inventory height in comparison to the experimental data is outstanding. Furthermore, detailed volume fraction and pressure profiles through the CFB are presented. Consequently, the S-shape characteristics of the solids fraction distribution in the riser reported by other researchers (Li et al., 1988; Louge and Chang, 1990) is verified through a detailed radial distribution of solids fraction and solids velocity through the riser.

These results validate the usefulness of CFD-DEM as a design tool, and verify that prediction accuracy requires faithful comparison to experimental data together with appropriate numerical model selection. Consequently, the MFIX model has demonstrated its value as a high-fidelity simulation tool, capable of predicting key performance parameters for challenging CFB flow conditions.

## 5. REFERENCES


Alder, B. J.; Wainwright, T. E. Phase Transition for a Hard Sphere System. *J. Chem. Phys.* **1957**, *27* (5), 1208–1209.

Ambler, P. A.; Milne, B. J.; Berruti, F.; Scott, D. S. Residence Time Distribution of Solids in a Circulating Fluidized Bed: Experimental and Modelling Studies. *Chem. Eng. Sci.* **1990**, *45* (8), 2179–2186.

Bader, R.; Findlay, J.; Knowlton, T. M. Gas/solid Flow Patterns in a 30.5 Cm Diameter Circulating Fluidized Bed. In *Circulating fluidized bed technology II*; 1988; pp 123–137.

Bai, D.-R.; Jin, Y.; Yu, Z.-Q.; Zhu, J.-X. The Axial Distribution of the Cross-Sectionally Averaged Voidage in Fast Fluidized Beds. *Powder Technol.* **1992**, *71* (1), 51–58.

Beetstra, R.; van der Hoef, M. A.; Kuipers, J. A. M. Numerical Study of Segregation Using a New Drag Force Correlation for Polydisperse Systems Derived from Lattice-Boltzmann Simulations. *Chem. Eng. Sci.* **2007**, *62* (1), 246–255.

Berruti, F.; Pugsley, T. S.; Godfroy, L.; Chaouki, J.; Patience, G. S. Hydrodynamics of Circulating Fluidized Bed Risers: A Review. *Can. J. Chem. Eng.* **1995**, *73* (5), 579–602.

Boerefijn, R.; Poletto, M.; Salatino, P. Analysis of the Dynamics of Heat Transfer between a Hot Wire Probe and Gas Fluidized Beds. *Powder Technol.* **1999**, *102* (1), 53–63.

Brereton, C. M. H.; Grace, J. R. Microstructural Aspects of the Behaviour of Circulating Fluidized Beds. *Chem. Eng. Sci.* **1993**, *48* (14), 2565–2572.

Buist, K. A.; van der Gaag, A. C.; Deen, N. G.; Kuipers, J. A. M. Improved Magnetic Particle Tracking Technique in Dense Gas Fluidized Beds. *AIChE J.* **2014**, *60* (9), 3133–3142.

Carlos Varas, A. E.; Peters, E. A. J. F.; Deen, N. G.; Kuipers, J. A. M. Solids Volume Fraction Measurements on Riser Flow Using a Temporal-Histogram Based DIA Method. *AIChE J.* **2016**, *62* (8), 2681–2698.

Cheng, Y.; Wei, F.; Yang, G.; Jin, Y. Inlet and Outlet Effects on Flow Patterns in Gas-Solid Risers. *Powder Technol.* **1998**, *98* (2), 151–156.

Dietiker, J. F.; Guenther, C.; Syamlal, M. A Cartesian Cut Cell Method for Gas/Solids Flow. In *AIChE annual meeting*; Nashville, TN, 2009.

Ding, J.; Gidaspow, D. A Bubbling Fluidization Model Using Kinetic Theory of Granular Flow. *AIChE J.* **1990**, *36* (4), 523–538.

Ellis, N.; Briens, L. A.; Grace, J. R.; Bi, H. T.; Lim, C. J. Characterization of Dynamic Behaviour in Gas–solid Turbulent Fluidized Bed Using Chaos and Wavelet Analyses. *Chem. Eng. J.* **2003**, *96* (1), 105–116.

Garg, R.; Galvin, J.; Li, T.; Pannala, S. Open-Source MFIX-DEM Software for Gas–solids Flows: Part I—Verification Studies. *Powder Technol.* **2012**, *220*, 122–137.

Gopalakrishnan, P.; Tafti, D. Development of Parallel DEM for the Open Source Code MFIX. *Powder Technol.* **2013**, *235*, 33–41.

Gopalan, B.; Shaffer, F. A New Method for Decomposition of High Speed Particle Image Velocimetry Data. *Powder Technol.* **2012**, *220*, 164–171.

Gopalan, B.; Shaffer, F. Higher Order Statistical Analysis of Eulerian Particle Velocity Data in CFB Risers as Measured with High Speed Particle Imaging. *Powder Technol.* **2013**, *242*, 13–26.

HILL, R. J.; KOCH, D. L.; LADD, A. J. C. The First Effects of Fluid Inertia on Flows in Ordered and Random Arrays of Spheres. *J. Fluid Mech.* **2001**, *448*, 213–241.

van der Hoef, M. A.; Ye, M.; van Sint Annaland, M.; Andrews, A. T.; Sundaresan, S.; Kuipers, J. A. M. Multiscale Modeling of Gas-Fluidized Beds. *Adv. Chem. Eng.* **2006**, *31*, 65–149.

Horio, M.; Kuroki, H. Three-Dimensional Flow Visualization of Dilutely Dispersed Solids in Bubbling and Circulating Fluidized Beds. *Chem. Eng. Sci.* **1994**, *49* (15), 2413–2421.

Ishii, H.; Nakajima, T.; Horio, M. The Clustering Annular Flow Model of Circulating Fluidized Beds. *J. Chem. Eng. JAPAN* **1989**, *22* (5), 484–490.

Jajcevic, D.; Siegmann, E.; Radeke, C.; Khinast, J. G. Large-Scale CFD–DEM Simulations of Fluidized Granular Systems. *Chem. Eng. Sci.* **2013**, *98*, 298–310.

Johnsson, F.; Zijerveld, R. .; Schouten, J. .; van den Bleek, C. .; Leckner, B. Characterization of Fluidization Regimes by Time-Series Analysis of Pressure Fluctuations. *Int. J. Multiph. Flow* **2000**, *26* (4), 663–715.

Kirkpatrick, M. P.; Armfield, S. W.; Kent, J. H. A Representation of Curved Boundaries for the Solution of the Navier–Stokes Equations on a Staggered Three-Dimensional Cartesian Grid. *J. Comput. Phys.* **2003**, *184* (1), 1–36.

Lackermeier, U.; Rudnick, C.; Werther, J.; Bredebusch, A.; Burkhardt, H. Visualization of Flow Structures inside a Circulating Fluidized Bed by Means of Laser Sheet and Image Processing. *Powder Technol.* **2001**, *114* (1), 71–83.

Levy, Y.; Lockwood, F. C. Laser Doppler Measurements of Flow in Freeboard of a Fluidized Bed. *AIChE J.* **1983**, *29* (6), 889–895.

Li, J.; Tung, Y.; Kwauk, M. Axial Voidage Profiles of Fast Fluidized Beds in Different Operating Regions. In *Circulating fluidized bed technology II*; 1988; pp 193–203.

Li, T.; Garg, R.; Galvin, J.; Pannala, S. Open-Source MFIX-DEM Software for Gas-Solids Flows: Part II — Validation Studies. *Powder Technol.* **2012**, *220*, 138–150.

Li, T.; Dietiker, J.-F.; Shadle, L. Comparison of Full-Loop and Riser-Only Simulations for a Pilot-Scale Circulating Fluidized Bed Riser. *Chem. Eng. Sci.* **2014**, *120*, 10–21.

Liu, H.; Tafti, D. K.; Li, T. Hybrid Parallelism in MFIX CFD-DEM Using OpenMP. *Powder Technol.* **2014**, *259*, 22–29.

Louge, M.; Chang, H. Pressure and Voidage Gradients in Vertical Gas-Solid Risers. *Powder Technol.* **1990**, *60* (2), 197–201.

Lu, B.; Zhang, N.; Wang, W.; Li, J.; Chiu, J. H.; Kang, S. G. 3-D Full-Loop Simulation of an Industrial-Scale Circulating Fluidized-Bed Boiler. *AIChE J.* **2013**, *59* (4), 1108–1117.

Lun, C. K. K.; Savage, S. B.; Jeffrey, D. J.; Chepurniy, N. Kinetic Theories for Granular Flow: Inelastic Particles in Couette Flow and Slightly Inelastic Particles in a General Flowfield. *J. Fluid Mech.* **1984**, *140* (1), 223.

Mathiesen, V.; Solberg, T.; Hjertager, B. H. An Experimental and Computational Study of

Multiphase Flow Behavior in a Circulating Fluidized Bed. *Int. J. Multiph. Flow* **2000**, *26* (3), 387–419.

Miller, A.; Gidaspow, D. Dense, Vertical Gas-Solid Flow in a Pipe. *AIChE J.* **1992**, *38* (11), 1801–1815.

Mohs, G.; Gryczka, O.; Heinrich, S.; Mörl, L. Magnetic Monitoring of a Single Particle in a Prismatic Spouted Bed. *Chem. Eng. Sci.* **2009**, *64* (23), 4811–4825.

Müller, C. R.; Holland, D. J.; Sederman, A. J.; Mantle, M. D.; Gladden, L. F.; Davidson, J. F. Magnetic Resonance Imaging of Fluidized Beds. *Powder Technol.* **2008**, *183* (1), 53–62.

Nikolopoulos, A.; Nikolopoulos, N.; Charitos, A.; Grammelis, P.; Kakaras, E.; Bidwe, A. R.; Varela, G. High-Resolution 3-D Full-Loop Simulation of a CFB Carbonator Cold Model. *Chem. Eng. Sci.* **2013**, *90*, 137–150.

Panday, R.; Breault, G.; Tucker, J.; Gopalan, B.; Higham, J.; Rogers, W. *Experimental Measurements of Small-Scale Circulating Fluidized Bed Performance for Model Validation*; NETL-PUB-21385; NETL Technical Report Series; U.S. Department of Energy, National Energy Technology Laboratory: Morgantown, WV, 2017.

Patience, G. S.; Chaouki, J. Gas Phase Hydrodynamics in the Riser of a Circulating Fluidized Bed. *Chem. Eng. Sci.* **1993**, *48* (18), 3195–3205.

Pugsley, T.; Lapointe, D.; Hirschberg, B.; Werther, J. Exit Effects in Circulating Fluidized Bed Risers. *Can. J. Chem. Eng.* **1997**, *75* (6), 1001–1010.

Reh, L.; Li, J. Measurement of Voidage in Fluidized Beds by Optical Probes. *Circ. Fluid. bed Technol.* **1991**, *3*, 105–113.

S. Ergun. Fluid Flow through Packed Columns. *Chem. Eng. Prog.* **1952**, *48*, 89–94.

Shaffer, F.; Gopalan, B.; Breault, R. W.; Cocco, R.; Karri, S. B. R.; Hays, R.; Knowlton, T. High Speed Imaging of Particle Flow Fields in CFB Risers. *Powder Technol.* **2013**, *242*, 86–99.

Shaffer, F. D. Method of Particle Trajectory Recognition in Particle Flows of High Particle Concentration Using a Candidate Trajectory Tree Process with Variable Search Areas, 2013.

van Sint Annaland, M.; Deen, N. G.; Kuipers, J. A. M. Numerical Simulation of Gas–liquid–solid Flows Using a Combined Front Tracking and Discrete Particle Method. *Chem. Eng. Sci.* **2005**, *60* (22), 6188–6198.

Syamlal, M. *MFIX Documentation: Numerical Technique*; 1998.

Syamlal, M.; Rogers, W.; O'brien, T. J. *MFIX Documentation: Theory Guide*; 1993.

Syamlal, M.; Rogers, W.; O'brien, T. J. *Summary of MFIX Equations*; 2012.

Tsuzuki, S.; Aoki, T. Large-Scale Particle Simulations for Debris Flows Using Dynamic Load Balance on a GPU-Rich Supercomputer. In *EGU General Assembly 2016, held 17-22 April, 2016 in Vienna Austria, p.4857*; 2016; Vol. 18, p 4857.

Walther, J. H.; Sbalzarini, I. F. Large-scale Parallel Discrete Element Simulations of Granular Flow. *Eng. Comput.* **2009**, *26* (6), 688–697.

Wang, J.; Ge, W.; Li, J. Eulerian Simulation of Heterogeneous Gas–solid Flows in CFB Risers: EMMS-Based Sub-Grid Scale Model with a Revised Cluster Description. *Chem. Eng. Sci.* **2008**, *63* (6), 1553–1571.

Wen, C. Y.; Yu, Y. H. A Generalized Method for Predicting the Minimum Fluidization Velocity. *AIChE J.* **1966**, *12* (3), 610–612.

Werther, J. Measurement Techniques in Fluidized Beds. *Powder Technol.* **1999**, *102* (1), 15–36.

Xiong, Q.; Li, B.; Zhou, G.; Fang, X.; Xu, J.; Wang, J.; He, X.; Wang, X.; Wang, L.; Ge, W.; et al. Large-Scale DNS of Gas–solid Flows on Mole-8.5. *Chem. Eng. Sci.* **2012**, *71*, 422–430.

Yang, S.; Luo, K.; Zhang, K.; Qiu, K.; Fan, J. Numerical Study of a Lab-Scale Double Slot-Rectangular Spouted Bed with the Parallel CFD–DEM Coupling Approach. *Powder Technol.* **2015**, *272*, 85–99.

Yerushalmi, J.; Cankurt, N. T.; Geldart, D.; Liss, B. Flow Regimes in Vertical Gas-Solid Contact Systems. In *Flow regimes in vertical gas-solid contact systems*; 1976.

Zhang, N.; Lu, B.; Wang, W.; Li, J. 3D CFD Simulation of Hydrodynamics of a 150MWe Circulating Fluidized Bed Boiler. *Chem. Eng. J.* **2010**, *162* (2), 821–828.

Zhang, W.; Wang, C.; Yang, W.; Wang, C.-H. Application of Electrical Capacitance Tomography in Particulate Process Measurement – A Review. *Adv. Powder Technol.* **2014**, *25* (1), 174–188.